AMERICAN METEOROLOGICAL SOCIETY

Journal of Physical Oceanography

EARLY ONLINE RELEASE

The DOI for this manuscript is doi: 10.1175/JPO-D-17-0111.1

Kopte, R., P. Brandt, M. Claus, R. Greatbatch, and M. Dengler, 2017: Role of Equatorial Basin-Mode Resonance for the Seasonal Variability of the Angola Current at 11°S. J. Phys. Oceanogr. doi:10.1175/JPO-D-17-0111.1, in press.

Role of Equatorial Basin-Mode Resonance for the Seasonal Variability of the Angola Current at 11°S

Robert Kopte[1], Peter Brandt[1,2], Martin Claus[1], Richard J. Greatbatch[1,2], and Marcus Dengler[1]

[1] GEOMAR Helmholtz Centre for Ocean Research Kiel, Kiel, Germany.

[2] Christian-Albrechts-Universität zu Kiel, Kiel, Germany.

November 28, 2017

Corresponding author: Robert Kopte, GEOMAR Helmholtz Centre for Ocean Research Kiel, Düsternbrooker Weg 20, 24105 Kiel, Germany.

E-mail: rkopte@geomar.de; Tel: +49 431 6004159

Abstract

Multi-year moored velocity observations of the Angola Current near 11°S reveal a weak southward mean flow superimposed by substantial intraseasonal to seasonal variability, including annual and semiannual cycles with distinct baroclinic structures. In the equatorial Atlantic these oscillations are associated with basin-mode resonances of the fourth and second baroclinic modes, respectively. Here, the role of basin-mode resonance and local forcing for the Angola Current seasonality are investigated. A suite of linear shallow-water models for the tropical Atlantic is employed, each model representing a single baroclinic mode forced at a specific period. The annually and semiannually oscillating forcing is given by 1) an idealized zonally uniform zonal forcing restricted to the equatorial band corresponding to a remote equatorial forcing or 2) realistic, spatially-varying Fourier components of wind stress data that include local forcing off Angola, particularly alongshore winds. Model-computed modal amplitudes are scaled to match moored velocity observations from the equatorial Atlantic. The observed annual cycle of alongshore velocity at 11°S is well reproduced by the remote equatorial forcing. Including local forcing slightly improves the agreement between observed and simulated semiannual oscillations at 11°S compared to the purely equatorial forcing. However, the model-computed semiannual cycle lacks amplitude at mid-depth. This could be the result of either underestimating the strength of the second equatorial basin-mode of the fourth baroclinic mode or other processes not accounted for in the shallow-water models. Overall, our findings underline the importance of large-scale linear equatorial wave dynamics for the seasonal variability of the boundary circulation off Angola.

Words: 250

1 Introduction

The Angola Current represents a major feature of the boundary circulation in the southeastern tropical Atlantic, connecting the equatorial Atlantic with the coastal upwelling systems of Angola and Benguela [*Peterson and Stramma*, 1991; *Rouault et al.*, 2007; *Ostrowski et al.*, 2009]. In the past, based exclusively on synoptic observations, the Angola Current had been assumed as a continuous poleward current, yet seasonally varying in strength, thereby advecting warm tropical waters southward [*Moroshkin et al.*, 1970; *Dias*, 1983b; a]. Since July 2013, two current meters have been in place on the continental slope near 11°S to investigate both advective and Coastally Trapped Wave (CTW) signals in the Angola Current [*Kopte et al.*, 2017]. These direct velocity observations revealed a strongly variable alongshore flow in the depth range between 45 and 450 m with periodically alternating poleward and equatorward velocities in the range of ±40 cm s^{-1} on submonthly to intraseasonal time scales. A weak southward mean flow was found in the upper 200 m representing the Angola Current with core velocities of 8 cm s^{-1} at about 50 m depth and an associated southward mean transport of 0.32 Sv [*Kopte et al.*, 2017]. Transport variability due to the semiannual and annual harmonics was determined to be of the same order as the mean Angola Current transport. The Angola Current converges with the northward flowing Benguela Current at about 16°S, where a sharp, yet highly variable thermal front is formed known as the Angola-Benguela Frontal Zone (ABFZ) [*Meeuwis and Lutjeharms*, 1990].

The ocean circulation off Southwestern Africa is highly sensitive to equatorial wave dynamics. Eastward propagating Equatorial Kelvin Waves (EKWs) are initiated by wind stress modulations in the equatorial Atlantic. Upon reaching the African coast, EKWs are reflected as westward propagating Rossby waves. Additionally, part of the EKW energy is transmitted into poleward

propagating CTWs. Downwelling CTWs are associated with poleward intrusions of warm tropical waters across the ABFZ eventually causing severe warm events in the northern Benguela [*Florenchie et al.*, 2003; *Lübbecke et al.*, 2010; *Bachèlery et al.*, 2016]. Owed to their similarities to the El Niño phenomenon in the Pacific Ocean, these intermittent warm events are referred to as Benguela Niños [*Shannon et al.*, 1986] and are known to have severe impact on the local marine ecosystem and rainfall variability affecting both fishery and agricultural sectors of the neighboring countries [*Gammelsrød et al.*, 1998]. Based on regional modeling studies excluding the seasonal cycle in the analysis, *Bachèlery et al.* [2016] attributed intraseasonal variability in the upwelling system mainly to local forcing, which is in agreement with an observational study of submonthly to intraseasonal sea surface temperature (SST) variability in the central Benguela upwelling region [*Goubanova et al.*, 2013]. Nonetheless, continuous and recurrent propagation of EKWs and CTWs from intraseasonal [*Polo et al.*, 2008] via seasonal [*Schouten et al.*, 2005; *Rouault*, 2012] to interannual time scales [*Bachèlery et al.*, 2016] are well documented from satellite altimetry data. Passages of these waves also imply modulations of the Angola Current strength through thermocline displacements [*Ostrowski et al.*, 2009]. Likewise in the Pacific, semiannual oscillations of the Peru-Chile Undercurrent in the south and the California Undercurrent in the north have been associated with the passage of semiannual CTWs that are induced by semiannual EKWs [*Pizarro et al.*, 2002; *Gómez-Valdivia et al.*, 2017]. Thermocline displacements associated with CTWs have been verified as far south as 21°S off the coast of Chile [*Ramos et al.*, 2006].

The main focus of the present study is the seasonal cycle of the Angola Current as observed by the moored current meters near 11°S. As the equatorial and coastal wave-guides are well connected, a question to be addressed is whether the variability observed in the Angola Current

is linked to equatorial Atlantic variability particularly on seasonal time scales. A large fraction of the observed variability in the equatorial Atlantic circulation is concentrated near resonance frequencies associated with equatorial basin modes [*Claus et al.*, 2016; *Brandt et al.*, 2016]. Equatorial basin modes [*Cane and Moore*, 1981] represent low-frequency standing equatorial modes in a zonally bounded basin and are composed of EKWs and long equatorial Rossby waves. While EKWs propagate eastward at a gravity wave speed associated with a particular baroclinic mode, long equatorial Rossby waves propagate westward with a speed three times slower than the corresponding EKW. Depending on the basin width $\boldsymbol{L}$ and the gravity wave speed $\boldsymbol{c_n}$ of the $\boldsymbol{n}$th baroclinic mode, the resonance periods of the respective basin mode are given by $\boldsymbol{T_{n,m} = 4 * L/(m * c_n)}$, where $\boldsymbol{m}$ is a positive integer, and $\boldsymbol{m = 1}$ corresponds to the gravest basin mode, while $\boldsymbol{m = 2}$ describes a second basin mode having one mid-basin nodal point (e.g. *Cane and Moore* [1981]; *Han et al.* [2011]). Despite weak wind forcing at the semiannual time scale in the equatorial Atlantic, a considerable semiannual cycle in equatorial circulation is found, which is attributed to the gravest basin mode of the second baroclinic mode excited by the resonance of this mode with the semiannual wind forcing [*Thierry et al.*, 2004; *Ding et al.*, 2009; *Brandt et al.*, 2016]. Likewise, the resonance period of the gravest basin mode for the fourth baroclinic mode is very close to the annual period, indicating resonance of this baroclinic mode with the annual wind forcing [*Brandt et al.*, 2016]. On interannual time scales, equatorial zonal flow variability is dominated by Equatorial Deep Jets (EDJs) and EDJs have been interpreted as equatorial basin modes for higher baroclinic modes [*Ascani et al.*, 2006; *d'Orgeville et al.*, 2007; *Greatbatch et al.*, 2012; *Claus et al.*, 2016].

The large-scale structure of the basin modes themselves, but also their role in exciting CTW propagation, suggests an impact of basin-mode-related dynamics on the boundary circulation off

Angola. This topic is investigated in the present study by employing multi-mode shallow-water simulations to reconstruct the observed seasonality of the Angola Current. A decomposition of moored zonal velocity observations acquired at 23°W-Equator [*Brandt et al.*, 2016] and at around 35°W-Equator [*Send et al.*, 2002; *Hormann and Brandt*, 2009] into baroclinic modes is aimed to the describe the gravest and second equatorial basin modes. Furthermore, these observations provide valuable information to scale model-computed modal amplitudes for each baroclinic mode at annual and semiannual frequencies.

The paper is organized as follows: In Section 2 the observational data sets used in this study are introduced, while Section 3 briefly describes an ocean general circulation model which will be compared to both observations and shallow-water model simulations. Section 4 introduces the basic equations, setup and forcing of the shallow-water model experiments. Section 5 is devoted to the model validation and baroclinic mode analysis in the equatorial band. In Section 6 observed and simulated annual and semiannual cycles at 11°S-Angola will be compared for various model experiments to examine the role of equatorial and local forcing for the seasonality of the Angola Current. A summary with a discussion of the results is presented in Section 7.

2 Observational Data

Off Angola, direct velocity observations are available from two successive deployment periods of an ADCP mooring from July 2013 to October 2016 (Figure 1). For each deployment, the mooring was located on the continental slope at ~1200 m water depth (13°11’E, 10°50’S), constituting the offshore component of a mooring array monitoring the boundary current flow off Angola [*Kopte et al.*, 2017]. The inshore component, a bottom shield deployed at ~500 m depth (13°11.0’E, 10°42.7’S), was lost during the second deployment period presumably due to fishing

activities. Therefore, in the following we primarily use ADCP data from the offshore mooring for a more robust description of the seasonality in the alongshore flow. The mooring configuration was identical during both deployment periods. An upward-looking 75-kHz Teledyne RDI's Workhorse Long Ranger ADCP was mounted to the mooring cable at 500 m depth. The instrument measured velocity in the water column up to about 45 m below the sea surface with a vertical resolution defined by a 16-m bin size.

As a proxy for near-surface velocities we use the delayed-time multi-mission ("all-sat-merged") product of absolute geostrophic velocities from AVISO. The dataset is provided with daily resolution on a 0.25° x 0.25° grid (details on the mapping algorithm of the altimetric observations can be found in *Pujol et al.* [2016]). The data are distributed by the E.U. Copernicus Marine Service Information (http://marine.copernicus.eu/). We extract velocity time series from the closest data point (13°07.5'E, 10°52.5'S) to the mooring position (Figure 1).

Additionally, for this study we make use of ocean velocity time series acquired along the equator at 23°W and 35°W. The 23°W-Equator time series comprises a multi-year record of equatorial zonal velocity obtained from current meters deployed between 2004 and 2016. Merging nine successive deployment periods, this product is an updated version of the one presented in *Brandt et al.* [2016]. It is composed of moored ADCPs profiling the upper 600-900 m of the water column, a few single-point current meters between 600 and 1000 m depth, as well as a McLane Moored Profiler (MMP) sampling between 1000 and 3500 m depth (for further details on the mooring setup see *Brandt et al.* [2016]). The time series used here also incorporates lowered-ADCP profiles taken during the mooring service cruises near the mooring position. Significantly fewer measurements are available at 35°W-Equator. Here, the merged time series of zonal velocity contains moored ADCP data covering the upper 550 m depth between August 2004 and

June 2006 [*Hormann and Brandt*, 2009] as well as data from three single-point current meters deployed at 652 m, 809 m, and 1107 m depth during the same period. Furthermore, deep velocity data are available at 36°W-Equator recorded by four single-point current meters at 1290 m, 1490 m, 1690 m, and 1890 m depth between October 1992 and June 1994, that previously have been used to study the space-time structure of the EDJs [*Send et al.*, 2002] and that are incorporated into the 35°W dataset. To improve the vertical coverage we incorporate nine lowered-ADCP as well as eight Pegasus profiles, that were acquired between 1°N/S at 35°W during several cruises and cover the seasonal cycle.

A 40-hour low-pass filter was applied to all available ADCP data (temporal resolution ranging from 2 to 8 h), as well as to single-point current meter data (temporal resolution of 2 h) to eliminate tidal currents. The MMP executed two successive profiles, an upcast followed by a downcast, every four or six days, with the two profiles separated by six hours. Here, no temporal filter was applied.

Finally, ADCP data from 11°S-Angola were linearly interpolated on a 1-day x 5-m grid, while the velocity data acquired by different instrument types at 23°W-Equator and 35°W-Equator were gridded onto a regular 15-day x 10-m grid. Note the different total lengths of velocity time series obtained at the mooring locations, with the 23°W-Equator mooring providing at least five years of zonal velocity data covering the whole water column, the 11°S-Angola mooring yielding about three years of boundary current observations, while at 35°W-Equator about two years of zonal velocity observations are available at distinct depth levels (Figure 2).

3 Ocean General Circulation Model TRATL01

For comparison with the observations and the shallow-water model experiments we use the fully-forced dynamical ocean general circulation model (OGCM) TRATL01 [*Duteil et al.*, 2014]. TRATL01 constitutes a 0.1° resolution nest between 30°S and 30°N in the Atlantic Ocean, that is embedded in a global ORCA05 configuration at 0.5° resolution via two-way-nesting [*Debreu and Blayo*, 2008]. The configuration is forced by interannually varying atmospheric data provided by the Coordinated Ocean-Ice Reference Experiments (CORE) v2 reanalysis data [*Griffies et al.*, 2009] over the period 1948-2007.

4 Shallow-water model simulations

To examine the role of remote equatorial versus local forcing as well as the potential impact of equatorial basin modes on the seasonality of the boundary circulation as observed at 11°S-Angola, we employ a suite of linear shallow-water models, each model representing the solution for a single baroclinic mode (e.g. *Gill* [1982]).

4.1 Basic equations

In spherical coordinates the governing equations associated with a particular baroclinic mode $\boldsymbol{n}$ are given by (see also *Greatbatch et al.* [2012]; *Zhu et al.* [2017]):

$$\frac{\partial \boldsymbol{u_n}}{\partial \boldsymbol{t}} - \boldsymbol{f v_n} = -\frac{\boldsymbol{g}}{\boldsymbol{a}\cos\boldsymbol{\theta}}\frac{\partial \boldsymbol{\eta_n}}{\partial \boldsymbol{\lambda}} + \frac{\boldsymbol{\tau_s^x}}{\boldsymbol{\rho H_E}}\boldsymbol{G_n} + \boldsymbol{F^u} \tag{1}$$

$$\frac{\partial \boldsymbol{v_n}}{\partial \boldsymbol{t}} + \boldsymbol{f u_n} = -\frac{\boldsymbol{g}}{\boldsymbol{a}}\frac{\partial \boldsymbol{\eta_n}}{\partial \boldsymbol{\theta}} + \frac{\boldsymbol{\tau_s^y}}{\boldsymbol{\rho H_E}}\boldsymbol{G_n} + \boldsymbol{F^v} \tag{2}$$

$$\frac{\partial \boldsymbol{\eta_n}}{\partial \boldsymbol{t}} + \frac{\boldsymbol{H_n}}{\boldsymbol{a}\cos\boldsymbol{\theta}}\left[\frac{\partial \boldsymbol{u_n}}{\partial \boldsymbol{\lambda}} + \frac{\partial(\cos\boldsymbol{\theta}\boldsymbol{v_n})}{\partial \boldsymbol{\theta}}\right] = \boldsymbol{0} \tag{3}$$

where $\boldsymbol{\theta}$ is latitude, $\boldsymbol{\lambda}$ is longitude, $\boldsymbol{a}$ is the radius of the earth, $\boldsymbol{f = 2\Omega \sin \theta}$ is the Coriolis parameter with $\boldsymbol{\Omega}$ being the angular speed of the earth, $\boldsymbol{g}$ is the acceleration due to gravity, $\boldsymbol{\rho}$ is a representative density for sea water. $\boldsymbol{u}$ and $\boldsymbol{v}$ correspond to the horizontal velocity components in the eastward and northward directions, respectively, while $\boldsymbol{\eta}$ represents the isopycnal displacement. $\boldsymbol{H_E}$ is a depth scale for the surface Ekman layer. $(\boldsymbol{F^u, F^v})$ is the lateral mixing of momentum given by

$$\boldsymbol{F^u = \frac{A_h}{a^2}\left[\frac{1}{\cos^2\theta}\frac{\partial^2 u}{\partial \lambda^2} + \frac{1}{\cos\theta}\frac{\partial}{\partial\theta}\left(\cos\theta\frac{\partial u}{\partial\theta}\right) + u(1-\tan^2\theta) - \frac{2\sin\theta}{\cos^2\theta}\frac{\partial v}{\partial\lambda}\right]} \quad (4)$$

$$\boldsymbol{F^v = \frac{A_h}{a^2}\left[\frac{1}{\cos^2\theta}\frac{\partial^2 v}{\partial \lambda^2} + \frac{1}{\cos\theta}\frac{\partial}{\partial\theta}\left(\cos\theta\frac{\partial v}{\partial\theta}\right) + v(1-\tan^2\theta) - \frac{2\sin\theta}{\cos^2\theta}\frac{\partial u}{\partial\lambda}\right]} \quad (5)$$

where $\boldsymbol{A_h}$ is the horizontal eddy viscosity coefficient. Furthermore, $\boldsymbol{H_n}$ is the equivalent depth set by the wave speed $\boldsymbol{c_n = \sqrt{gH_n}}$ associated with baroclinic mode $\boldsymbol{n}$. $\left(\boldsymbol{\tau_s^x, \tau_s^y}\right)$ represents the surface wind stress vector that acts as a body force with $\boldsymbol{G_n}$ representing the wind stress projection coefficient for each baroclinic mode. Choosing an approach similar to *Zhu et al.* [2017], we first solve the equations for $\boldsymbol{G_n = 1}$, and then obtain realistic projection coefficients by fitting model-computed modal amplitudes to modal amplitudes derived from observed velocities at 23°W-Equator (see section 5.1 and section 5.3).

4.2 Model setup and forcing

We set up a model domain for the Atlantic Ocean extending from 60°W to 15°E in the zonal and from 34°S to 25°N in the meridional direction. The 1000 m isobath represents the coastline. Both model boundaries and coastlines are treated as solid vertical walls. Along the northern and southern boundaries of the model domain sponge layers with e-folding scale of 2.5° latitude are

applied to inhibit Kelvin wave propagation. The model has a horizontal resolution of 0.25° both in longitude and latitude. The scale depth $\boldsymbol{H_E}$ is chosen to be 500 m, which is an arbitrary choice, as the actual value of $\boldsymbol{H_E}$ will only affect the scaling factor $\boldsymbol{G_n}$ in the fitting procedure. Lateral eddy viscosity is set to $\boldsymbol{A_h = 300\ m^2 s^{-1}}$ [*Claus et al.*, 2014; *Brandt et al.*, 2016].

Model simulations are carried out with varying gravity wave speeds representing the first five baroclinic modes. Either annually or semiannually oscillating forcing is applied to the momentum equations with each shallow-water model being run for 11 years, which is sufficient for the model to reach equilibrium near the equator. The oscillating solution of the eleventh integration year is stored for further analysis. In order to distinguish between the role of the equatorial forcing that eventually excites resonant equatorial basin modes and the role of local forcing off Angola, we carry out two sets of simulations that differ in the applied forcing.

In the first set of model simulations, the forcing is derived from oscillating wind stress (including both the zonal and meridional components) applied to the entire model domain. These runs therefore include the equatorial forcing (EF) potentially exciting equatorial basin modes as well as any local forcing (LF) that might be relevant at 11°S-Angola (hereafter referred to as "EF+LF"). Equivalent runs are carried out using four different wind products with differing horizontal resolutions (Table 1). For consistency, annual and semiannual wind stress cycles are calculated from wind stress data between March 2007 and June 2016 for each wind product.

In a second set of simulations, the model is forced by a zonally uniform zonal forcing oscillating at either annual or semiannual frequency and restricted to the equatorial band (hereafter referred to as "EF-only"). Following *Greatbatch et al.* [2012], the forcing ($\boldsymbol{\tau_s^x}$ in Equation (1)) is given by

$$\tau_s^x = X_0 e^{-\left(\frac{\beta y^2}{2c_n}\right)} \sin(\omega t) \quad (6)$$

where $y = a\theta$, $\beta = 2.3 \times 10^{-11}\, m^{-1}s^{-1}$ is the meridional gradient of *f* at the equator, $\omega = 2\pi/T_B$ is the forcing frequency with T_B being either the annual or semiannual period, and X_0 being the amplitude. The results are independent of the choice of the amplitude, as the model-computed modal amplitudes (as well as the phases) from the EF-only runs are adjusted to reach agreement with the EF+LF runs at 23°W-Equator. By excluding the local forcing at the eastern boundary, the EF-only runs assist in evaluating the relative importance of remote equatorial and local forcing for the seasonality of the eastern boundary circulation off Angola.

5. Baroclinic mode analysis and model validation in the equatorial band

5.1 Modal decomposition of observed zonal velocity at the equator

As noted in section 4.1, the projection coefficients G_n are not assumed a priori, but remain to be determined through the fitting of model-computed modal amplitudes to modal amplitudes derived from the time series of top-to-bottom zonal velocity at 23°W-Equator. The mooring location at 23°W-Equator appears advantageous for estimating the amplitudes of the gravest basin modes [*Brandt et al.*, 2016]. Here we use the vertical structure functions, $\hat{p}_n(z)$, of the first five baroclinic modes representing a subset of those derived by *Claus et al.* [2016] for an ocean depth of H = 4500 m (Figure 3a). They were calculated from a mean buoyancy frequency profile obtained from 47 shipboard CTD profiles acquired near 23°W-Equator during the mooring service cruises. The structure functions of the low baroclinic modes change only marginally when taking into account the variability about the mean buoyancy frequency profile. Note that the structure functions have been normalized so that $\frac{1}{H}\int_{-H}^{0}(\hat{p}_n(z))^2 dz = 1$.

The modal decomposition of observed zonal velocity at 23°W-Equator is carried out by consecutively projecting the vertical structures associated with one particular baroclinic mode (Figure 3a) multiplied with either the annual or semiannual cycle onto the velocity time series. As the time series contains some gaps particularly at deeper levels, the orthogonality of the projected modes is not ensured. Therefore, the first 20 baroclinic modes are fitted in random order with the resulting contribution of the corresponding baroclinic mode being subtracted from the velocity signal before fitting the next mode. Repeating this procedure for 10000 random permutations of the fitting order yields estimates of the most probable mode energies and phases and associated uncertainties (Figure 3b). To test the robustness particularly with regard to the phase distribution, the modal decomposition is carried out once for annual and semiannual components derived using the total length of the time series and once using only the 2013-2016 period, with the latter corresponding to the mooring observation period at 11°S-Angola. We note the dominance of the fourth baroclinic mode for the annual cycle and the second baroclinic mode for the semiannual cycle as discussed by *Brandt et al.* [2016], but also the stability of these modes in terms of energy and phase lock when comparing results from different observation periods (Figure 3b). However, a relative increase of the energy associated with the third and fourth baroclinic mode for the annual cycle of up to 25 percent is found when considering the 2013-2016 period, while the phases remain unchanged. Here, an anomalously deep reaching Equatorial Undercurrent during the second half of 2015 (not shown) most likely results in an enhanced projection of the annual cycle onto these modes. For the semiannual cycle of the second baroclinic mode the energy varies by about 20 percent for the limited period relative to the value obtained for the full time series, while the phase stays within less than 8 days.

Nevertheless, overall we find a consistent mode energy-phase distribution for both annual and semiannual cycles derived using different reference periods.

A similar study conducted in the Indian Ocean [*Han et al.*, 2011] has indicated the potential importance of second basin modes, which are characterized by a nodal point in mid-basin. In the Atlantic, 23°W-Equator is located in the proximity of this amplitude minimum, which complicates the description of a second basin mode based on velocity data from 23°W-Equator. Therefore, the modal decomposition is also carried out for the velocity time series acquired at 35°W-Equator (Figure 3c). As the latter is limited both in temporal and vertical coverage, the modal characteristics are determined for the first five baroclinic modes only, based on 120 random permutations of the fitting order. Similar to 23°W-Equator, the fourth and second baroclinic modes are found to be dominating the annual and semiannual cycle, respectively. Interestingly, at 35°W-Equator the second baroclinic mode at the semiannual period exhibits highest energy, while the dominance of the fourth baroclinic mode at the annual period seems not as striking as at 23°W-Equator. However, given the comparably sparse sampling particularly of the deep ocean, uncertainties of derived amplitudes and phases are substantially larger at 35°W than at 23°W (Figure 3b, c).

5.2 Adjustment of prescribed gravity wave speeds in shallow-water model experiments

As a starting point for the shallow-water model experiments, a first realization of simulations driven by JRA-55 wind stress data [Japan Meteorological Agency, 2013] was obtained using gravity wave speeds as in Brandt et al. [2016] (Table 2). We then carried out five sensitivity experiments for each baroclinic mode by slightly modifying the prescribed phase speeds, aiming at improving the agreement between observed and model-computed modal phases at 23°W-

Equator (Figure 4 and Table 2). Note that $\boldsymbol{G_n}$=1 for the sensitivity experiments, as the choice of the wind projection coefficients does not influence the model-computed modal phases. The approach of adjusting prescribed gravity wave speeds is justified, as several factors not accounted for in the linear shallow-water model might affect the gravity wave speed such as background mean flow and nonlinear effects. Moreover, the gravity wave speed is treated as being constant across the basin by our model – a simplification that cannot be met in reality due to large-scale changes in stratification and mean flow. Gravity wave speeds for the first and fifth baroclinic mode remain unchanged. An improved agreement of observed and model-computed semiannual cycle is found for the second baroclinic mode when increasing the gravity wave speed by 0.11 m s^{-1} and for third baroclinic mode when decreasing the gravity wave speed by 0.06 m s^{-1}. These adjustments only marginally change the phase differences for the corresponding annual cycles. Likewise, decreasing the gravity wave speed of the fourth baroclinic mode by 0.06 m s^{-1} minimizes the phase difference for the annual cycle (Figure 4). 5.3 Scaling of model-computed modal amplitudes and choice of wind forcing product

Oscillation amplitudes obtained from the modal decompositions at 23°W-Equator (section 5.1) are now used to quantify the wind stress projection coefficients $\boldsymbol{G_n}$ separately for annual and semiannual oscillations. $\boldsymbol{G_n}$ is determined as the ratio of modal amplitudes of the zonal velocity derived from observations and the corresponding model-computed modal amplitudes from the EF+LF runs at 23°W-Equator. While model-computed modal amplitudes are scaled, modal phases are determined solely by the model, i.e. are not fitted to match the observed modal phases at 23°W-Equator.

A set of equivalent EF+LF shallow-water model simulations is carried out differing only by the applied wind forcing product (Table 1) in order to assess the dependency of the model runs on

the chosen forcing product to reproduce the seasonal cycle of zonal velocity along the equator. The derived wind stress projection coefficients $\boldsymbol{G_n}$, which correspond to the scaling factor for model-computed modal amplitudes, provide a measure on how much energy input is needed to reproduce observed amplitudes of annual and semiannual oscillations. Therefore, $\boldsymbol{G_n}$ is not only a function of the wind energy input, but also depends critically on how realistically the model reproduces the resonance characteristics (see also *Greatbatch et al.* [2012]; *Brandt et al.* [2016]). The latter depend on several parameters of the model configuration such as basin geometry, dissipation and gravity wave speeds. A comparison of wind stress projection coefficients depending on the wind forcing product and the oscillation period does reveal a clustering for coefficients derived from scaling model-computed modal amplitudes at 23°W-Equator for similar baroclinic modes and oscillation periods (Figure 5a). In general, there is only a weak dependence on the chosen forcing product. However, some larger differences between the products for particular baroclinic modes should be noted. For example, the coefficients for the second baroclinic mode, annual cycle or the fourth baroclinic mode, semiannual cycle associated with ERA/INTERIM forcing are about a factor three smaller or larger compared to the corresponding coefficients associated with the other forcing products. This means that a different energy input is necessary to reproduce the observed amplitudes for the corresponding baroclinic modes when forcing the model with oscillating wind stress derived from ERA/INTERIM compared to the other wind products. As our EF+LF model simulations differ only in the applied wind forcing, the findings demonstrate the uncertainties in the representation of specific aspects of the equatorial Atlantic circulation when forcing ocean models with one particular wind-forcing product. Similar projection coefficients are derived from scaling model-computed modal amplitudes at 35°W-Equator, which can differ significantly from their counterparts at 23°W-

Equator (Figure 5a). These differences might result partly from the less robust modal decomposition at 35°W-Equator and, in case of the gravest basin mode, from the mooring being located in an area of strongly changing and lower modal amplitudes (Figure 8 and 13).

Model-computed phases from EF+LF runs are not fitted to observations. Therefore, the difference of observed and simulated phases represents another indicator on how well the models are able to reproduce observed annual and semiannual oscillations locally at 23°W-Equator depending on the applied wind-forcing product (Figure 5b). Again, concerning the phase differences only minor dependencies on the applied wind forcing are found at least for baroclinic modes with significant energy at 23°W-Equator (compare Figure 3b). Phase differences at 35°W-Equator are generally larger (Figure 5b), as expected keeping in mind that gravity wave speeds are optimized for local agreement at 23°W-Equator. Yet again, smallest phase differences are observed for the dominant baroclinic modes that are close to basin-mode resonance. For the remainder of the study we decided on comparing simulations forced by annual and semiannual oscillations derived from the JRA-55 wind stress data and scaled locally at 23°W-Equator to our observations from the equatorial moorings and 11°S-Angola, as these simulations generally yield the best phase agreement to the observations at 23°W-Equator (for corresponding projection coefficients see Table 3). However we note, although the model-computed modal amplitudes are scaled to match observed modal amplitudes at 23°W-Equator, elsewhere they do depend on several aspects of the model configuration, such as the applied damping or the capture of the resonance characteristics as a function of basin geometry and chosen phase speeds.

To focus on the relative importance of equatorial and local forcing, modal amplitudes and phases from the EF-only runs are fitted to the scaled modal amplitudes and unaltered phases from the EF+LF runs at 23°W-Equator. Following this approach, EF+LF and EF-only runs agree locally

at 23°W-Equator, and differences between EF+LF runs and EF-only runs at 11°S-Angola can be related to the impact of local forcing that is retained in the EF+LF runs.

5.4 Validation of model-computed annual and semiannual cycles of zonal velocity at the equator

As a first test for our chosen set of EF+LF simulations, we compare the observed vertical structure of annual and semiannual cycles both at 23°W-Equator and 35°W-Equator to the sum of corresponding shallow-water model simulations for the first five baroclinic modes (Figure 6). The observed annual cycle of zonal velocity at 23°W-Equator (Figure 6a) is characterized by a phase jump at 70 to 80 m depth accompanied by maximum annual amplitudes above and below, mirroring the annual cycle in EUC core depth [*Brandt et al.*, 2016]. Deeper in the water column, significant annual amplitudes are found down to about 2500 m water depth. For comparison, we extract zonal velocities at the model grid point corresponding to 23°W-Equator from the EF+LF simulations. The scaled model-computed amplitude for each baroclinic mode is multiplied with the corresponding equatorial vertical structure function. The resulting time series of velocity profiles associated with each baroclinic mode are summed up to reconstruct the annual and semiannual cycles of zonal velocity. The sum of annually oscillating shallow-water model simulations for the first five baroclinic modes reveals a very similar behavior, showing zero amplitude at 70-80 m depth surrounded by maxima above and below (Figure 6b), however not as vertically confined as in the observations (Figure 6a). According to Figure 3b the pattern of annual amplitudes is mainly determined by the fourth baroclinic mode. However, due to discrepancies in the model-computed phases particularly for the third and fifth baroclinic mode (Figure 5b), a phase shift in the distribution of annual amplitudes is clearly visible compared to the observations. The observed vertical structure of semiannual amplitudes at 23°W-Equator (Figure 6e) is dominated by the second baroclinic mode (Figure 3b, *Brandt et al.* [2016]) and

accordingly is characterized by near-surface amplitude maxima. Below, compared to the annual cycle, the vertical structure is less baroclinic, consistent with the dominance of lower baroclinic modes. The reconstruction using semiannually oscillating shallow-water model simulations shows a very similar amplitude distribution compared to the observations both in magnitude and phase (Figure 6f). This is attributable to the precise simulation of the second baroclinic mode with the remaining modes having only minor influence on the semiannual cycle. In fact, for the semiannual cycle baroclinic modes 1, 3, 4, and 5 are characterized by energies of less than 0.7 $cm^2\ s^{-2}$, while the second baroclinic mode exhibits about 2.3 $cm^2\ s^{-2}$ (Figure 3b). Nevertheless, we note that the reconstructed semiannual cycle from shallow-water model simulations lacks structure and amplitude in the deep ocean below 1500 m depth.

A similar comparison is carried out for annual and semiannual components in zonal velocity at 35°W-Equator (Figure 6 c, d and g, h, respectively). Note again that projection coefficients obtained at 23°W-Equator are used for scaling of model-computed modal amplitudes. For the annual cycle, this results in a weaker simulated annual cycle with maximum near-surface amplitudes about 50 percent smaller compared to the observations. Despite the deficiencies in the strength of the simulated annual cycle near the surface, observed and model-computed baroclinic structures bear important similarities particularly in the structure and phasing of the variability at depth. The model-computed semiannual cycle at 35°W-Equator also suffers from a lack of near-surface amplitude (about 20 percent smaller compared to the observations). Apart from that, the largest differences are found in the depth range between 100 and 500 m depth, where the semiannual cycle reconstructed from observations shows stronger baroclinicity and higher amplitudes. At depth, observed and model-computed semiannual cycles largely agree in terms of the phasing, but with weaker model-computed amplitudes. Overall, larger discrepancies

418 are found for the reconstruction of observed and model-computed annual and semiannual
419 oscillations at 35°W-Equator compared to 23°W-Equator. These might partly be explained by
420 generally larger differences between observed and model-computed phases at 35°W-Equator
421 (Figure 5b). Furthermore we note the larger uncertainties in the reconstruction of observed
422 annual and semiannual cycles at 35°W-Equator, as it relies on less than two years of velocity
423 observations (Figure 2).

424 Nonetheless, our findings encourage us to evaluate the models further for their basin-wide
425 structures and particularly at 11°S-Angola.

426 **6 Seasonal cycle of the Angola Current**

427 6.1 Harmonic amplitudes of observed alongshore velocity at 11°S-Angola

428 While the annual component is the main contributor to the seasonal cycle of zonal velocity at
429 23°W-Equator [*Brandt et al.*, 2016], at 11°S-Angola the relative importance of the semiannual
430 compared to the annual cycle of alongshore velocity is strongly enhanced (Figure 7).
431 Furthermore, the periodogram derived by harmonic fits to the velocity data from the first
432 deployment period of the inshore ADCP off Angola reveals a strong component near 120 days.
433 However, this peak is neither as pronounced in the periodogram calculated from the first
434 deployment period for the offshore ADCP (not shown) nor in the periodogram for the offshore
435 ADCP when combining both deployment periods. Here, distinct peaks are found near 90 and 100
436 days, most likely associated with a period of enhanced intraseasonal variability in the alongshore
437 flow between December 2015 and April 2016 (Figure 1). In the following we restrict our
438 analysis to annual and semiannual oscillations, making use of the longer time series obtained

from the offshore ADCP. However, a brief discussion of the intraseasonal oscillations is provided in Section 7.

6.2 Horizontal structure of annual and semiannual oscillations

In a next step we explore the horizontal distribution of the amplitude of simulated annual and semiannual oscillations (Figure 8) in order to identify baroclinic modes relevant at 11°S off Angola. For this purpose we use the EF-only simulations that show the impact of purely equatorial forcing off the coast of Angola. The horizontal structures are generally characterized by elongated amplitude maxima along the equator; in the eastern part of the basin regions of enhanced amplitude are partly being deflected to the south. Largest amplitudes are obtained for the semiannual cycle of the second baroclinic mode and for the annual cycle of the fourth baroclinic mode, both showing maximum amplitude of zonal velocity oscillation at the equator in mid-basin. As discussed in *Brandt et al.* [2016], for these combinations of baroclinic mode and forcing period the equatorial ocean is close to resonance, forming gravest equatorial basin modes. Similar simulations for a rectangular ocean basin resulted in meridionally symmetric amplitude structures [*Brandt et al.*, 2016; *Han et al.*, 2011]. Including a realistic coastline generates asymmetric structures due to the presence of the Gulf of Guinea and the northwestward slanted coastline of equatorial Brazil. The horizontal structures of the amplitude for other combinations of baroclinic mode and forcing period can strongly deviate from the basin-mode structure (see, e.g., patterns of the first baroclinic mode). For the fourth baroclinic mode, semiannual cycle a different pattern is found, which is characterized by two amplitude maxima along the equator separated by a nodal point in mid-basin. It can be associated with a second basin mode. In any case, enhanced amplitudes of higher baroclinic modes are more confined to the equator in their meridional extent (Figure 8). Note that Figure 8 displays the amplitudes of

462 the baroclinic mode contribution to the surface velocity, where the second baroclinic mode has
463 the largest expression (compare Figure 3a). In the subsurface the relative importance of different
464 baroclinic modes varies depending on their vertical structure. Off the coast of Southwestern
465 Africa alongshore velocities have a dominant meridional component. Therefore, the amplitude of
466 the meridional velocity is displayed in the southeastern corner of the domain in Figure 8.
467 Whether a particular baroclinic mode affects the velocity at 11°S-Angola apparently depends on
468 the meridional extent and associated shape of the southward deflection of the amplitude
469 maximum as well as on the mode's energy as determined at 23°W-Equator. The fourth and
470 second baroclinic modes, being found to dominate the annual and semiannual cycles in zonal
471 velocity both at 23°W-Equator and 35°W-Equator, respectively, also appear to dominate the
472 annual and semiannual cycles in meridional velocity at 11°S-Angola. Simulations for baroclinic
473 modes closest to basin-mode resonance are generally found to exhibit appropriate amplitudes to
474 influence the meridional velocity near the coast at 11°S, i.e. baroclinic modes 3-5 and 1-3 for the
475 annual and semiannual cycle, respectively. However, for the semiannual cycle the near-coastal
476 amplitude maximum of meridional velocity is located south of 11°S-Angola for the first and
477 second baroclinic modes suggesting an even stronger impact of the equatorial forcing further
478 away from the equator. Particularly the first baroclinic mode exhibits low amplitude at the
479 semiannual period at 11°S-Angola. Instead, the second basin mode of the fourth baroclinic mode
480 is likely to play a role.

481 6.3 Annual and semiannual cycles of alongshore velocity at 11°S-Angola

482 The annual and semiannual components at 11°S-Angola are derived by fitting annual and
483 semiannual harmonics to the time series of alongshore velocity at each depth level (Figure 9a
484 and e, respectively). In agreement with Figure 7, the semiannual cycle on average shows higher

amplitudes compared to the annual cycle, along with a reduced baroclinicity. Annual and semiannual components derived from the corresponding time series of altimetry-based geostrophic velocities allow for the interpretation of near-surface baroclinic structures. For the annual cycle the flow reverses direction between the surface and the depth of the uppermost ADCP measurements (about 50 m). The semiannual cycle of the alongshore velocity is instead characterized by a more gradual change with depth, again indicating the dominance of low baroclinic modes. As for zonal velocity along the equator, the annual and semiannual cycles of alongshore velocity at 11°S-Angola are reconstructed by summing up the individual contributions of the first five baroclinic modes to the alongshore velocity extracted from the shallow-water model simulations. For the purely equatorial forcing, the model-computed annual cycle agrees well with the observations in terms of both amplitude and phase (Figure 9b, red line in Figure 10a, b). Thus, the annual cycle of alongshore velocity at 11°S-Angola appears to reflect primarily the response to the remote equatorial forcing. The purely equatorial forcing also generates a semiannual cycle at 11°S-Angola with a depth-averaged amplitude comparable to the observations (Figure 9f). However, the vertical structure and phasing of the model-computed semiannual cycle is substantial different compared to the observed one, characterized by too-strong near-surface velocities along with a phase difference of about two month and too-weak velocities at depth (red line in Figure 10c, d). This suggests that the remote equatorial forcing alone is not sufficient to set up the baroclinic structure of the semiannual cycle as observed, instead other driving processes such as local forcing might play a role as well. Therefore, a similar extraction is carried out for the EF+LF simulations that include also the local forcing along the eastern boundary. Again, using the first five baroclinic modes for the reconstruction of the annual cycle we find a good agreement between the summed-up model output (Figure 9c,

508 solid blue line in Figure 10a, b) and the observations (Figure 9a, black line in Figure 10a, b). The
509 reconstructed baroclinic structure of the semiannual cycle from the EF+LF simulations (Figure
510 9g, solid blue line in Figure 10c, d) is only marginally improved compared to the EF-only runs
511 (Figure 9f, red line in Figure 10c, d) with more realistic amplitudes of near-surface velocity and
512 an improved phasing. Nonetheless, mid-depth amplitudes are too weak also in the EF+LF runs,
513 and particularly do not indicate a local maximum as in the observations. In general, the inclusion
514 of local forcing introduces only small improvements for the model-computed semiannual cycle
515 compared to the runs with purely equatorial forcing. This indicates that additional processes not
516 included in our linear shallow-water model simulations must to some extent control the
517 semiannual cycle at 11°S-Angola. However, the baroclinic structure of the semiannual cycle of
518 the alongshore velocity at 11°S-Angola in the OGCM TRATL01 also shows similar
519 discrepancies compared to the observations, like too-strong near-surface velocity and a vertical
520 phase distribution that agrees better with the shallow-water model runs than the observations
521 (green lines in Figure 10c, d). Nonetheless, in TRATL01 a mid-depth maximum of semiannual
522 amplitudes is indicated, although slightly deeper and not as pronounced as in the observations
523 (Figure 10c). For the annual cycle from TRATL01, we note a slightly deeper depth of both the
524 phase transition (Figure 10b) and the mid-depth maximum (Figure 10a) compared to the
525 observed annual cycle. Overall, we find a general good agreement between observations,
526 shallow-water model simulations, and TRATL01 for the annual cycle. We further note
527 substantial differences in the observed and model-computed semiannual cycle. As the
528 discrepancies are (partly) present in both shallow-water model simulations and TRATL01
529 potential causes are not easy to assess.

530 To further evaluate the importance of the remote equatorial forcing particularly for the annual
531 cycle at 11°S-Angola, the amplitude and phase of the individual modal contributions to the
532 oscillation are compared between the simulations driven with equatorial forcing and those
533 simulations driven with full forcing. With few exceptions modal phase differences for the two
534 sets of simulations are within less than one month and modal amplitude differences are smaller
535 than 0.1 cm s^{-1} (Table 4). These minor differences underline the dominance of the remote
536 equatorial forcing for the annual cycle at 11°S-Angola. The larger discrepancy between the
537 reconstructions of the forcing-dependent semiannual cycles is largely associated with the third
538 baroclinic mode, which is phase-shifted by about one month, and, more importantly, stronger in
539 amplitude by about 0.23 cm s^{-1} in the simulation with equatorial forcing only. Multiplied with the
540 corresponding vertical structure function (Figure 3a), this difference in amplitude is sufficient to
541 explain the intensification near the surface and concurrent reduction at depth in the semiannual
542 cycle reconstructed from simulations based on equatorial forcing compared to the simulations
543 with realistic forcing (Figure 9f).

544 As Figure 8 suggests, in general only baroclinic modes with basin-mode resonance periods close
545 to either the annual or semiannual cycles are likely to influence the alongshore velocity off the
546 coast of Angola. Therefore, we repeat the reconstruction using EF+LF simulations summing up
547 only selected baroclinic modes, which are modes 3-5 and 1-3 for the annual and semiannual
548 cycles, respectively (Figure 9d and h). As expected from Figure 8, the annual cycle is only little
549 changed compared to the reconstruction using five modes, stressing the importance of the fourth
550 baroclinic mode for the annual cycle with contributions from both the third and fifth baroclinic
551 modes especially in setting up the phases. For the semiannual cycle, the restriction to the first
552 three baroclinic modes results in even less amplitude at mid-depth. Together with Figure 8 and

10, this indicates the influence of higher baroclinic modes in generating the observed baroclinic structure of the semiannual cycle in alongshore velocity at 11°S-Angola and thus, besides the gravest basin mode, also a potential impact of the second basin mode for the fourth baroclinic mode.

7 Summary and discussion

We have analyzed the seasonal cycle of alongshore velocity measured by a moored ADCP at 11°S-Angola between July 2013 and October 2016. Pronounced spectral peaks at annual and semiannual frequencies (Figure 7) were found to be associated with distinct baroclinic structures (Figure 9a, e). In the equatorial Atlantic resonant basin modes [*Cane and Moore*, 1981] have been found to represent robust features that are associated with pronounced spectral peaks in zonal velocity time series at the annual and semiannual frequencies [*Claus et al.*, 2016; *Brandt et al.*, 2016; *Thierry et al.*, 2004; *Ding et al.*, 2009]. Equatorial basin modes are composed of equatorial Kelvin and long equatorial Rossby waves for a particular baroclinic mode, with basin resonances found at characteristic periods depending on both gravity wave speed and basin geometry. Given the link between the equatorial and coastal wave-guides, we examine the relative importance of remote equatorial forcing including potential basin-mode resonances versus the local forcing off Angola for the observed annual and semiannual cycle of alongshore velocity at 11°S-Angola.

A suite of shallow-water model simulations is employed, forced either by zonally uniform oscillating zonal forcing restricted to the equatorial band (EF-only runs) or by the Fourier components of several wind products corresponding to the annual and semiannual periods (EF+LF runs). Model-computed modal amplitudes are fitted to modal amplitudes derived from

mooring data at 23°W-Equator (Figure 5a and Table 3). Note that the resulting wind stress projection coefficients may differ for annual and semiannual frequencies for the same baroclinic mode. As noted earlier, it is crucial how well our simulations capture the resonance characteristics of the equatorial Atlantic [*Greatbatch et al.*, 2012; *Brandt et al.*, 2016]. The resonance frequency in the model depends mainly on the combination of chosen gravity wave speed and model boundary geometry. Furthermore, dissipation of wave energy could be different for the annual and semiannual cycle, but is prescribed and fixed in the shallow-water model simulations. Therefore, the wind stress projection coefficients do not so much mirror the wind energy input (and are therefore not necessarily similar for different oscillation periods), but rather indicate how much energy input is required to establish similar modal amplitudes as observed at a given oscillation period, given the model-inherent resonance characteristics.

The large-scale horizontal structures of the amplitude of annual and semiannual oscillations for different baroclinic modes suggest their dynamic influence on the boundary circulation off Angola (Figure 8). In model simulations driven with zonally uniform zonal forcing restricted to the equatorial band (EF-only) the observed annual cycle of alongshore velocity at 11°S-Angola is already well reproduced, suggesting remote equatorial forcing as the major driver for annual oscillations of the eastern boundary circulation off Angola (Figure 9b). Although the remote equatorial forcing also generates a semiannual cycle of comparable amplitude, the model-computed semiannual cycle is significantly different from the observed one (Figure 9f). Some improvements in terms of the vertical structure and phase of the reconstructed semiannual cycle are achieved when including local forcing along the eastern boundary (EF+LF runs, Figure 9g). Furthermore, it could be shown that both simulated annual and semiannual oscillations appear to

be primarily determined by those baroclinic modes being close to basin-mode resonance either for the annual or semiannual frequency (Figure 9d, h).

Nevertheless, while amplitudes of model-derived and observed annual cycles are very similar, the model-derived semiannual cycle lacks amplitude at mid-depth. Given the vertical structure of the baroclinic modes (Figure 3a), contributions of higher baroclinic modes seem to be underestimated for the semiannual cycle. Here we want to note that our approach for scaling model-computed modal amplitudes relies on one particular location in the central equatorial Atlantic, where an observational data set of top-to-bottom ocean velocities is available to allow for baroclinic mode decomposition. However, owing to the differences in the spatial distribution of the amplitude for different baroclinic modes, a locally confined scaling might be problematic, as seen for example for the fourth baroclinic mode, semiannual cycle. The corresponding basin mode represents the structure of a second basin mode, which is characterized by two velocity maxima along the equator (Figure 8). 23°W-Equator is located close to the nodal point of the second basin mode, which complicates the determination of the corresponding modal amplitude and thus adds uncertainty to the scaling of model-computed modal amplitudes. By artificially enhancing the amplitude of the fourth baroclinic mode it can be tested whether a larger contribution of this mode improves the model-computed semiannual cycle. More specifically this would require that the model-determined phase of the fourth mode at 11°S-Angola allows for an improvement of the baroclinic structure of the semiannual cycle. Enhancing the amplitude of the fourth baroclinic mode, semiannual cycle, e.g. by a factor 4.5 indeed leads to an improvement of the phasing of the model-computed semiannual cycle (Figure 11b). However, although the semiannual cycle at mid-depth is slightly enhanced, amplitudes are still substantially different compared to the observations (Figure 11a). Overall, this indicates that the phase of the

620 semiannual cycle of the fourth baroclinic mode as determined by our simulation would permit a
621 stronger contribution of this mode and a limiting factor for a realistic reconstruction of the
622 semiannual cycle at 11°S-Angola appears to be the amplitude of the fourth baroclinic mode.
623 Here, the modal decomposition derived from zonal velocity data at 35°W-Equator yields another
624 estimate of the strength of the second basin mode associated with the fourth baroclinic mode,
625 semiannual cycle. Indeed, the mode energy for this particular basin mode is found to be
626 significantly larger at 35°W-Equator compared to 23°W-Equator (0.25 $cm^2\ s^{-2}$ vs. 0.08 $cm^2\ s^{-2}$).
627 However, the corresponding scaling coefficients for the shallow-water model simulations
628 derived independently at the two locations are very similar (0.09 at 35°W-Equator vs. 0.07 at
629 23°W-Equator, compare Table 3). Hence, the strength of the simulated basin mode associated
630 with the fourth baroclinic, semiannual cycle would change only marginally, if we scaled our
631 simulations at 35°W-Equator and thus cannot explain the too-weak amplitude at 11°S-Angola.

632 However, several other factors potentially influence the model-computed amplitude at 11°S-
633 Angola. Among them are model-inherent characteristics such as the applied damping and the
634 efficiency of basin-mode resonance depending on model geometry and chosen phase speeds. As
635 noted earlier, gravity wave speeds are kept constant in our simulations. Consequently, large-scale
636 changes in stratification (e.g. due to the eastward shoaling and thinning of the equatorial
637 thermocline) that might cause changing wave speeds as well as scattering of baroclinic waves are
638 not taken into account in the model. According to *Clarke and Van Gorder* [1986] scattering of
639 baroclinic waves also occurs via frictional coupling, which depends on the bottom topography
640 (in case of CTWs on the shelf slope steepness). However, our model setup does not contain
641 topographic features like the mid-Atlantic ridge and treats coastlines as solid vertical walls.
642 Therefore, the potential transfer of energy between baroclinic modes is not included in our

model. Also the interaction of equatorial waves with the mean flow as discussed by *Claus et al.* [2014] for high-order baroclinic modes is not included in our model. Furthermore, linear models also do not include nonlinear processes like a potential nonlinear interaction of the annual cycle with itself that could shift energy to the semiannual cycle. In this way, the dominant basin mode of the annual cycle, being of fourth baroclinic mode, might feed energy into the second basin mode of the semiannual cycle, providing one potential explanation for the missing strength of the fourth baroclinic mode in the semiannual cycle in our linear model. Nevertheless, given the simplicity of our model, it seems even more remarkable how much of the annual and, with some reservations, semiannual oscillations discussed here appear to be governed essentially by linear dynamics.

While investigating the seasonal cycle of equatorial Atlantic circulation, *Brandt et al.* [2016] compared their shallow-water, basin-mode simulations to the ocean general circulation model (OGCM) TRATL01 [*Duteil et al.*, 2014], noting similarities in the representation of the dominant basin modes for the annual and semiannual cycles. As for zonal velocity at 23°W-Equator, annual and semiannual cycles of alongshore velocity at 11°S-Angola bear important similarities between observations and TRATL01 (Figure 10). However, local maxima/minima or phase transitions are generally found slightly deeper in TRATL01 compared to the observations, pointing to a too-strong vertical diffusion in the model [*Brandt et al.*, 2016]. Considering baroclinic mode contributions, this would result in a stronger projection onto the third instead of the fourth baroclinic mode (not shown). Thus, for the semiannual cycle it still supports the potential importance of the fourth baroclinic mode in setting up the semiannual cycle of alongshore velocity at 11°S-Angola. A modal decomposition of zonal velocity from TRATL01 at 23°W-Equator qualitatively confirms the importance of particular baroclinic modes as seen in

the observations, nonetheless the annual cycle of the fourth baroclinic mode is more energetic while the semiannual cycle of the second baroclinic mode is less energetic in TRATL01 (Figure 12b). Similar to 11°S-Angola, the relative contribution of the third baroclinic mode to the annual cycle is larger in TRATL01 compared to the observations at 23°W-Equator. At 35°W-Equator the third baroclinic mode is the largest contributor to the annual cycle in TRATL01, while the modal decomposition of the observed time series suggests local dominance of the fourth baroclinic mode followed by the second baroclinic mode (Figure 12a). Considering the semiannual cycle at 35°W-Equator, the large amplitude of the second baroclinic mode derived from observations is mirrored neither by TRATL01 nor by the EF+LF shallow-water model simulations scaled at 23°W-Equator. Overall, mode energy spectra derived from observations, the EF+LF shallow-water model runs, and TRATL01 agree less well at 35°W-Equator compared to 23°W-Equator. As noted earlier, the uncertainties associated with the modal decomposition of the zonal velocity observations at 35°W-Equator are rather large and might be one of the factors accounting for the differences between mode spectra. Furthermore, for a realistic representation of the seasonal cycle of the equatorial circulation by an OGCM it seems crucial that resonance characteristics are captured correctly. To achieve the latter, a realistic representation of the stratification along the equator is essential, as this specifies corresponding gravity wave speeds. While our shallow-water model simulations assume constant phase speeds across the basin, TRATL01 does account for changes in stratification. Consequently, the basin-wide structures of the annual and semiannual cycles for a specific baroclinic mode can look significantly different in TRATL01 compared to our idealized simulations (Figure 14). Comparably small shifts in the location of local maxima thus can result in rather large discrepancies in the modal amplitude at one particular location, as seen for example in the annual cycle of the second baroclinic mode

near 35°W (compare Figure 8 and Figure 14). Also the location of local maxima associated with the semiannual cycle of the fourth baroclinic mode is significantly different between the shallow-water model simulations and TRATL01, underlining the problematic nature of correctly scaling modal amplitudes relying on individual locations, where suitable observations are available.

The CTW response of the coastal upwelling regions off Angola and Namibia to the remote equatorial wind forcing has previously been discussed mainly with respect to the intermittent occurrence of warm Benguela Niño events [*Florenchie et al.*, 2003; *Florenchie et al.*, 2004; *Rouault et al.*, 2007; *Huang and Hu*, 2007; *Lübbecke et al.*, 2010; *Richter et al.*, 2010; *Bachèlery et al.*, 2016] developing in the northern Benguela. Carrying out a set of regional model simulations for the Southeast Atlantic intentionally excluding the seasonal cycle in the analysis, *Bachèlery et al.* [2016] noted the dominance of remote equatorial forcing on interannual time scales while on intraseasonal time scales local forcing prevailed. However, for seasonal time scales particularly the importance of the semiannual cycle as contributor to upwelling and downwelling seasons off Angola has been underlined [*Ostrowski et al.*, 2009; *Rouault*, 2012; *Kopte et al.*, 2017]. The mooring observations off Angola (Figure 1) for the first time reveal the baroclinic structures of both the annual and semiannual cycle and our results appear to confirm that equatorial dynamics play a crucial role for the eastern boundary circulation variability on these time scales.

As noted in section 6.1 on intraseasonal time scales a pronounced spectral peak in the velocity time series is found near 120 days for the inshore ADCP (Figure 7). The persistence of this oscillation cannot be verified with the available data. Nevertheless, elevated energy near 120 days is also found in the zonal velocity time series at 23°W-Equator, which might be associated with resonance of either the gravest basin mode of the first baroclinic mode or the second basin

712 mode of the second baroclinic mode. The vertical structure of the 120-day oscillation at 11°S-
713 Angola indeed suggests the dominance of low baroclinic modes (not shown). Interestingly, a
714 basin resonance at 120-day has been described for the Caribbean Sea [*Hughes et al.*, 2016], that
715 could impact also equatorial Atlantic circulation via CTW and EKW response and potentially
716 even the boundary circulation off Angola. However, the isolation of the corresponding signatures
717 in the velocity data at 23°W-Equator was hindered by several interfering, stronger signals that
718 are associated with a diversity of forcing mechanisms. Thus, the possible equatorial forcing of
719 intraseasonal variability in the boundary circulation off Angola remains an open question.

720

721 **Acknowledgments and Data**

722 This study was supported by the German Federal Ministry of Education and Research as part of
723 the SACUS project (03G0837A), by European Union 7th Framework Programme (FP7 2007–
724 2013) under grant agreement 603521 PREFACE project, and by the Deutsche
725 Forschungsgemeinschaft as part of the Sonderforschungsbereich 754 (SFB754) “Climate- and
726 Biogeochemistry Interactions in the Tropical Atlantic”. Moored velocity observations at 23°W-
727 Equator were acquired in cooperation with the PIRATA project, with additional support for the
728 moored profiler observations provided by the U. S. National Science Foundation. We thank the
729 captains and crew of the R/V *Meteor*, R/V *Maria S. Merian*, and R/V *L’Atalante* as well as our
730 technical group for their help with the fieldwork. Furthermore, we thank F. P. Tuchen for helpful
731 discussions. F. U. Schwarzkopf, C. W. Böning, and the Kiel ocean modeling group developed
732 TRATL01 as part of the European DRAKKAR collaboration. JRA-55 reanalysis data were
733 provided by the NCAR/UCAR Research Data Archive, accessible via http://rda.ucar.edu/ under
734 data set number ds628.0. ASCAT data are produced by Remote Sensing Systems and sponsored

by the NASA Ocean Vector Winds Science Team. Data are available at http://www.remss.com. ERA-Interim reanalysis data are produced by the European Centre for Medium-Range Weather Forecasts (ECMWF) and available through http://apps.ecmwf.int/datasets/data/interim-full-daily/levtype=sfc/. NCEP-DOE AMIP-II reanalysis data were provided by the NOAA/OAR/ESRL PSD, Boulder, Colorado, United States. It can be accessed via http://www.esrl.noaa.gov/psd/. Furthermore, the study has been conducted using E.U. Copernicus Marine Service Information by accessing altimetry data available at http://marine.copernicus.eu/.

744 **References**
745
746 Ascani, F., D. Wang, and E. Firing (2006), Equatorial deep jets in a simple ocean generation
747 circulation model, Eos Trans. AGU, 87(36), Ocean Sci. Meet. Suppl., Abstract OS33C-05.

748 Bachèlery, M.-L., S. Illig, and I. Dadou (2016), Interannual variability in the South-East Atlantic
749 Ocean, focusing on the Benguela Upwelling System: Remote versus local forcing, J Geophys
750 Res-Oceans, 121(1), 284-310, doi: 10.1002/2015JC011168.

751 Berrisford, P., D. P. Dee, K. Fielding, M. Fuentes, P. W. Kållberg, S. Kobayashi, and S. Uppala
752 (2009), The ERA-Interim archive, in *ERA Report Series*, edited, p. 16, ECMWF, Shinfield Park,
753 Reading.

754 Brandt, P., M. Claus, R. J. Greatbatch, R. Kopte, J. M. Toole, W. E. Johns, and C. W. Böning
755 (2016), Annual and Semiannual Cycle of Equatorial Atlantic Circulation Associated with Basin-
756 Mode Resonance, J Phys Oceanogr, 46(10), 3011-3029, doi: 10.1175/jpo-d-15-0248.1.

757 Cane, M. A., and D. W. Moore (1981), A Note on Low-Frequency Equatorial Basin Modes, J
758 Phys Oceanogr, 11(11), 1578-1584, doi: 10.1175/1520-
759 0485(1981)011<1578:ANOLFE>2.0.CO;2.

760 Clarke, A. J., and S. Van Gorder (1986), A Method for Estimating Wind-Driven Frictional,
761 Time-Dependent, Stratified Shelf and Slope Water Flow, J Phys Oceanogr, 16(6), 1013-1028,
762 doi: 10.1175/1520-0485(1986)016<1013:AMFEWD>2.0.CO;2.

763 Claus, M., R. J. Greatbatch, and P. Brandt (2014), Influence of the Barotropic Mean Flow on the
764 Width and the Structure of the Atlantic Equatorial Deep Jets, J Phys Oceanogr, 44(9), 2485-
765 2497, doi: 10.1175/jpo-d-14-0056.1.

766 Claus, M., R. J. Greatbatch, P. Brandt, and J. M. Toole (2016), Forcing of the Atlantic Equatorial
767 Deep Jets Derived from Observations, J Phys Oceanogr, 46(12), 3549-3562, doi: 10.1175/jpo-d-
768 16-0140.1.

769 d'Orgeville, M., B. L. Hua, and H. Sasaki (2007), Equatorial deep jets triggered by a large
770 vertical scale variability within the western boundary layer, J Mar Res, 65(1), 1-25, doi:
771 10.1357/002224007780388720.

772 Debreu, L., and E. Blayo (2008), Two-way embedding algorithms: a review, Ocean Dynam,
773 58(5), 415-428, doi: 10.1007/s10236-008-0150-9.

774 Dias, C. A. (1983a), Preliminary report on the physical oceanography off southern Angola,
775 March and July 1971, Collection of Scientific Papers International Commission for the Southeast
776 Atlantic Fisheries, 10, 103-116.

Dias, C. A. (1983b), Note on the evidence of a permanent southward flow of the upper oceanic tropospheric waters off Angola at 12°S, Collection of Scientific Papers International Commission for the Southeast Atlantic Fisheries, 10, 99-102.

Ding, H., N. S. Keenlyside, and M. Latif (2009), Seasonal cycle in the upper equatorial Atlantic Ocean, Journal of Geophysical Research: Oceans, 114(C9), C09016, doi: 10.1029/2009JC005418.

Duteil, O., F. U. Schwarzkopf, C. W. Böning, and A. Oschlies (2014), Major role of the equatorial current system in setting oxygen levels in the eastern tropical Atlantic Ocean: A high-resolution model study, Geophys Res Lett, 41(6), 2033-2040, doi: 10.1002/2013gl058888.

Florenchie, P., J. R. E. Lutjeharms, C. J. C. Reason, S. Masson, and M. Rouault (2003), The source of Benguela Niños in the South Atlantic Ocean, Geophys Res Lett, 30(10), doi: 10.1029/2003GL017172.

Florenchie, P., C. J. C. Reason, J. R. E. Lutjeharms, M. Rouault, C. Roy, and S. Masson (2004), Evolution of Interannual Warm and Cold Events in the Southeast Atlantic Ocean, J Climate, 17(12), 2318-2334, doi: 10.1175/1520-0442(2004)017<2318:eoiwac>2.0.co;2.

Gammelsrød, T., C. H. Bartholomae, D. C. Boyer, V. L. L. Filipe, and M. J. O'Toole (1998), Intrusion of warm surface water along the Angolan-Namibian coast in February–March 1995: the 1995 Benguela Nino, South African Journal of Marine Science, 19(1), 41-56, doi: 10.2989/025776198784126719.

Gill, A. E. (1982), Atmosphere-Ocean Dynamics, 662 pp., Academic Press, San Diego, California.

Gómez-Valdivia, F., A. Parés-Sierra, and A. Laura Flores-Morales (2017), Semiannual variability of the California Undercurrent along the Southern California Current System: A tropical generated phenomenon, Journal of Geophysical Research: Oceans, 122(2), 1574-1589, doi: 10.1002/2016JC012350.

Goubanova, K., S. Illig, E. Machu, V. Garçon, and B. Dewitte (2013), SST subseasonal variability in the central Benguela upwelling system as inferred from satellite observations (1999–2009), Journal of Geophysical Research: Oceans, 118(9), 4092-4110, doi: 10.1002/jgrc.20287.

Greatbatch, R. J., P. Brandt, M. Claus, S. H. Didwischus, and Y. Fu (2012), On the width of the equatorial deep jets, J Phys Oceanogr, 42(10), 1729-1740, doi: 10.1175/Jpo-D-11-0238.1.

Griffies, S. M., et al. (2009), Coordinated Ocean-ice Reference Experiments (COREs), Ocean Model, 26(1–2), 1-46, doi: 10.1016/j.ocemod.2008.08.007.

Han, W., J. P. McCreary, Y. Masumoto, J. Vialard, and B. Duncan (2011), Basin Resonances in the Equatorial Indian Ocean, J Phys Oceanogr, 41(6), 1252-1270, doi: 10.1175/2011jpo4591.1.

Hormann, V., and P. Brandt (2009), Upper equatorial Atlantic variability during 2002 and 2005 associated with equatorial Kelvin waves, J Geophys Res-Oceans, 114, doi: 10.1029/2008jc005101.

Huang, B., and Z.-Z. Hu (2007), Cloud-SST feedback in southeastern tropical Atlantic anomalous events, Journal of Geophysical Research: Oceans, 112(C3), C03015, doi: 10.1029/2006JC003626.

Hughes, C. W., J. Williams, A. Hibbert, C. Boening, and J. Oram (2016), A Rossby whistle: A resonant basin mode observed in the Caribbean Sea, Geophys Res Lett, 43(13), 7036-7043, doi: 10.1002/2016GL069573.

Japan Meteorological Agency, J. (2013), JRA-55: Japanese 55-year Reanalysis, Daily 3-Hourly and 6-Hourly Data, edited, Research Data Archive at the National Center for Atmospheric Research, Computational and Information Systems Laboratory, Boulder, CO.

Johnson, E. R. (1991), The Scattering at Low Frequencies of Coastally Trapped Waves, J Phys Oceanogr, 21(7), 913-932, doi: 10.1175/1520-0485(1991)021<0913:TSALFO>2.0.CO;2.

Kanamitsu, M., J. Ebisuzaki, J. Woollen, S. K. Yang, J. J. Hnilo, M. Fiorino, and G. L. Potter (2002), NCEP–DOE AMIP-II Reanalysis (R-2), B Am Meteorol Soc, 83(11), 1631-1643, doi: 10.1175/bams-83-11-1631.

Kopte, R., P. Brandt, M. Dengler, P. C. M. Tchipalanga, M. Macuéria, and M. Ostrowski (2017), The Angola Current: Flow and hydrographic characteristics as observed at 11°S, Journal of Geophysical Research: Oceans, 122(2), 1177-1189, doi: 10.1002/2016JC012374.

Lübbecke, J. F., C. W. Böning, N. S. Keenlyside, and S.-P. Xie (2010), On the connection between Benguela and equatorial Atlantic Niños and the role of the South Atlantic Anticyclone, J Geophys Res-Oceans, 115(C9), doi: 10.1029/2009JC005964.

Meeuwis, J. M., and J. R. E. Lutjeharms (1990), Surface thermal characteristics of the Angola-Benguela front, South African Journal of Marine Science, 9(1), 261-279, doi: 10.2989/025776190784378772.

Moroshkin, K. V., V. A. Bunov, and R. P. Bulatov (1970), Water circulation in the eastern South Atlantic Ocean, Oceanology, 10, 27-34.

Ostrowski, M., J. C. B. da Silva, and B. Bazik-Sangolay (2009), The response of sound scatterers to El Niño- and La Niña-like oceanographic regimes in the southeastern Atlantic, ICES Journal of Marine Science: Journal du Conseil, 66(6), 1063-1072, doi: 10.1093/icesjms/fsp102.

Peterson, R. G., and L. Stramma (1991), Upper-level circulation in the South Atlantic Ocean, Progress in Oceanography, 26(1), 1-73, doi: 10.1016/0079-6611(91)90006-8.

Pizarro, O., G. Shaffer, B. Dewitte, and M. Ramos (2002), Dynamics of seasonal and interannual variability of the Peru-Chile Undercurrent, Geophys Res Lett, 29(12), 22-21-22-24, doi: 10.1029/2002GL014790.

Polo, I., A. Lazar, B. Rodriguez-Fonseca, and S. Arnault (2008), Oceanic Kelvin waves and tropical Atlantic intraseasonal variability: 1. Kelvin wave characterization, J Geophys Res-Oceans, 113(C7), 18, doi: 10.1029/2007jc004495.

Pujol, M. I., Y. Faugère, G. Taburet, S. Dupuy, C. Pelloquin, M. Ablain, and N. Picot (2016), DUACS DT2014: the new multi-mission altimeter data set reprocessed over 20 years, Ocean Sci., 12(5), 1067-1090, doi: 10.5194/os-12-1067-2016.

Ramos, M., O. Pizarro, L. Bravo, and B. Dewitte (2006), Seasonal variability of the permanent thermocline off northern Chile, Geophys Res Lett, 33(9), L09608, doi: 10.1029/2006GL025882.

Ricciardulli, L., and F. J. Wentz (2016), Remote Sensing Systems ASCAT C-2015 Daily Ocean Vector Winds on 0.25 deg grid, Version 02.1, edited, Remote Sensing Systems, Santa Rosa, CA.

Richter, I., S. K. Behera, Y. Masumoto, B. Taguchi, N. Komori, and T. Yamagata (2010), On the triggering of Benguela Niños: Remote equatorial versus local influences, Geophys Res Lett, 37(20), L20604, doi: 10.1029/2010GL044461.

Rouault, M. (2012), Bi-annual intrusion of tropical water in the northern Benguela upwelling, Geophys Res Lett, 39(12), L12606, doi: 10.1029/2012GL052099.

Rouault, M., S. Illig, C. Bartholomae, C. J. C. Reason, and A. Bentamy (2007), Propagation and origin of warm anomalies in the Angola Benguela upwelling system in 2001, Journal of Marine Systems, 68(3–4), 473-488, doi: 10.1016/j.jmarsys.2006.11.010.

Schouten, M. W., R. P. Matano, and T. P. Strub (2005), A description of the seasonal cycle of the equatorial Atlantic from altimeter data, Deep Sea Research Part I: Oceanographic Research Papers, 52(3), 477-493, doi: 10.1016/j.dsr.2004.10.007.

Send, U., C. Eden, and F. Schott (2002), Atlantic Equatorial Deep Jets: Space–Time Structure and Cross-Equatorial Fluxes, J Phys Oceanogr, 32(3), 891-902, doi: 10.1175/1520-0485(2002)032<0891:aedjst>2.0.co;2.

872 Shannon, L. V., A. J. Boyd, G. B. Brundrit, and J. Taunton-Clark (1986), On the existence of an
873 El Niño-type phenomenon in the Benguela System, J Mar Res, 44(3), 495-520, doi:
874 10.1357/002224086788403105.

875 Thierry, V., A.-M. Treguier, and H. Mercier (2004), Numerical study of the annual and semi-
876 annual fluctuations in the deep equatorial Atlantic Ocean, Ocean Model, 6(1), 1-30, doi:
877 10.1016/S1463-5003(02)00054-9.

878 Zhu, X., R. J. Greatbatch, and M. Claus (2017), Interannual variability of tropical Pacific sea
879 level from 1993 to 2014, Journal of Geophysical Research: Oceans, 122(1), 602-616, doi:
880 10.1002/2016JC012347.
881

882

Table 1: Wind products used for forcing the EF+LF shallow-water model simulations. Crosses in column "BF" indicate when wind stress data was calculated based on available wind speed data via bulk formula $\vec{\tau} = \rho_a \cdot c_D \cdot \vec{u}_{10}^2$ with $\rho_a = 1.22\ kg\ m^{-3}$ and $c_D = 0.0013$.

Table 2: Gravity wave speeds c_n (m s^{-1}) for baroclinic modes 1-5 used in the shallow-water model simulations. In brackets gravity wave speeds as used in *Brandt et al.* [2016] are shown. See also Figure 4.

Table 3: Dimensionless wind stress projection coefficients G_n for EF+LF simulations being forced by Fourier components of JRA55 wind stress data corresponding to annual (middle column) and semiannual (right column) oscillations as obtained from scaling model-computed amplitudes locally at 23°W-Equator. In brackets corresponding wind stress projection coefficients derived from scaling model-computed amplitudes locally at 35°W-Equator are displayed.

Table 4: Amplitude and phase differences between EF-only and EF+LF simulations for individual baroclinic modes at 11°S-Angola. Positive/negative differences correspond to a stronger/weaker response to EF-only forcing compared to the EF+LF forcing, with the former inducing a southward maximum of surface alongshore velocity later/earlier, respectively. To obtain depth-dependent differences, the amplitude difference needs to be multiplied with the corresponding vertical structure function (Figure 3a).

905 **Figure 1:** Time series of alongshore velocity (rotated by -34° with respect to true north) as
906 recorded by the moored ADCP located on the 1200 m isobath off Angola (13°11.0'E,
907 10°50.0'S). Positive and negative values indicate equatorward and poleward flow, respectively.
908 The vertical dashed line marks the date of the mooring redeployment. Surface values correspond
909 to geostrophic alongshore velocities at the mooring location from altimetry.
910
911 **Figure 2:** Length of the time series of available velocity data as function of depth for 23°W-
912 Equator (blue), 11°S-Angola (orange), and 35°W-Equator (red).
913
914 **Figure 3:** (a) Vertical structure functions of the first five baroclinic modes derived from a mean
915 buoyancy frequency profile calculated from CTD profiles near 23°W-Equator. Normalization is
916 carried out with respect to the standard deviations of the structure functions. Modal amplitudes
917 of the energy of annual (squares, "AC") and semiannual (diamonds, "SAC") cycles of the
918 observed zonal velocity at 23°W-Equator (b) and 35°W-Equator (c) are plotted at the mode's
919 time of maximum eastward surface velocity. Note that, for the sake of clarity, only one of the
920 two maxima of the semiannual cycle is shown in (b) and (c). Errorbars correspond to standard
921 deviations of energy and phase accounting for uncertainties due to incomplete data sets (for
922 details on the mode projection see text). In (b) mode projection is carried out considering the full
923 length of the time series (filled symbols) as well as a subset of the time series (open symbols)
924 that corresponds to the period of moored observations at 11°S-Angola (2013-2016).
925
926 **Figure 4:** Local phase differences between observed and model-computed annual (squares,
927 "AC") and semiannual (diamonds, "SAC") cycles at 23°W-Equator as function of the prescribed

928 gravity wave speed for the first five baroclinic modes of EF+LF runs forced with JRA-55
929 oscillating wind stress. Vertical solid colored lines correspond to gravity wave speeds used for
930 the remainder of the study, vertical dashed black lines are associated with theoretical gravity
931 wave speeds used in *Brandt et al.* [2016]. See also Table 2.
932
933 **Figure 5:** (a) Dimensionless projection coefficients G_n for EF+LF simulations being forced by
934 different wind products. Projection coefficients are computed by fitting model-computed
935 amplitudes to amplitudes derived from projecting the corresponding baroclinic mode on annual
936 ("AC") and semiannual ("SAC") cycles of observed zonal velocity at 23°W-Equator (yellow and
937 red, respectively), and 35°W-Equator (only shown for JRA55 forcing, green and blue,
938 respectively). Model-computed phases are not fitted but remain solely determined by the applied
939 wind forcing and model characteristics. In (b) local phase differences between EF+LF shallow-
940 water model simulations and observed modal semiannual and annual cycles are shown; colors
941 and symbols as given in (a).
942
943 **Figure 6:** Annual ("AC") and semiannual ("SAC") cycles of zonal velocity (cm s^{-1}) at 23°W-
944 Equator and 35°W-Equator as reconstructed by fitting annual (a and c) and semiannual (e and g)
945 harmonics to the observed velocity field, and by summing up the first 5 baroclinic modes from
946 the EF+LF shallow-water model simulations forced with annually (b and d) and semiannually (f
947 and h) oscillating wind stress. Solid and dotted contours represent the +2 cm s^{-1} and -2 cm s^{-1}
948 isolines, respectively. Model-computed modal amplitudes are scaled with respect to observations
949 obtained at 23°W-Equator.
950

951 **Figure 7:** Mean periodograms of observed alongshore velocity at 11°S-Angola for the offshore
952 (red, 2013-2016) and inshore (blue, 2013-2015) ADCP. Periodograms are calculated by fitting
953 harmonic functions to the time series at each depth level between 45 and 450 m followed by
954 vertical averaging. Shaded areas indicate standard deviations of individual periodograms with
955 respect to depth.
956
957 **Figure 8:** Amplitudes of annual (left column, "AC") and semiannual (right column, "SAC")
958 cycles of surface zonal velocities for baroclinic modes 1-5 from the EF-only runs. Within the
959 rectangle in the southeastern corner of the domain corresponding amplitudes of meridional
960 velocity are shown (associated with the red color scale). Black dots denote mooring locations at
961 35°W-Equator, 23°W-Equator, and 11°S-Angola.
962
963 **Figure 9:** Baroclinic structures of observed annual (a, "AC") and semiannual (e, "SAC")
964 oscillations of alongshore velocity at 11°S-Angola derived by fitting harmonic functions at each
965 depth level. At the surface corresponding oscillations derived from AVISO geostrophic
966 velocities are shown. Shown to the right are corresponding baroclinic structures obtained from
967 the sum of the first five baroclinic modes from the EF-only simulations driven (b, f) and the
968 EF+LF simulations (c, g). In (d) and (h) only EF+LF simulations for baroclinic modes with their
969 resonance periods closest to either the annual or semiannual cycle are considered for the
970 summation. Solid and dotted contours in all subplots represent the +1 cm s^{-1} and -1 cm s^{-1}
971 isolines, respectively.
972

973 **Figure 10:** (left) Amplitude and (right) month of maximum northward flow, as function of depth
974 for (a and b) annual and (c and d) semiannual cycles of alongshore velocity at 11°S-Angola
975 corresponding to patterns in Figure 9: Observations (black), EF-only (red), and EF+LF
976 simulations (solid blue: Modes 1-5; dotted blue: Modes 3-5 for AC, modes 1-3 for SAC).
977 Additionally, corresponding profiles derived from TRATL01 output are shown in green.
978
979 **Figure 11:** (a) Amplitude and (b) phase as function of depth for semiannual cycle of alongshore
980 velocity at 11°S-Angola for observations (thick black), EF+LF simulations (dotted blue), and
981 EF+LF simulations, where the amplitude of the fourth baroclinic mode was enhance by a factor
982 4.5 (solid blue)
983
984 **Figure 12:** Baroclinic mode energy spectra of the annual (solid, "AC") and semiannual (dashed,
985 "SAC") cycles for 35°W-Equator (a) and 23°W-Equator (b) derived from moored velocity
986 observations (blue), EF+LF shallow-water model simulations (red), and the TRATL01 model
987 (green). In b) mode spectra of the shallow-water model are identical to the one derived from
988 observations as model-computed modal amplitudes are scaled locally at 23°W-Equator.
989
990 **Figure 13:** As Figure 8, but from the TRATL01 model. Mode projection is carried out at model
991 grid points with water depth larger than 1000 m.
992

Wind product	**Horiz. resolution (°)**	**BF**	**Reference**
JRA-55	0.5	x	*Japan Meteorological Agency* [2013]
ASCAT	0.25	x	*Ricciardulli and Wentz* [2016]
ERA/Interim	0.25		*Berrisford et al.* [2009]
NCEP-DOE AMIPII	~1.9	x	*Kanamitsu et al.* [2002]

Table 1: Wind products used for forcing the EF+LF shallow-water model simulations. Crosses in column "BF" indicate when wind stress data was calculated based on available wind speed data via bulk formula $\vec{\tau} = \rho_a \cdot c_D \cdot \vec{u}_{10}^2$ with $\rho_a = 1.22\ kg\ m^{-3}$ and $c_D = 0.0013$.

Baroclinic mode n	**Gravity wave speed c_n** (m s^{-1})
1	2.47 (2.47)
2	1.43 (1.32)
3	0.89 (0.95)
4	0.68 (0.74)
5	0.57 (0.57)

998

999 **Table 2:** Gravity wave speeds c_n (m s^{-1}) for baroclinic modes 1-5 used in the shallow-water
1000 model simulations. In brackets gravity wave speeds as used in *Brandt et al.* [2016] are shown.
1001 See also Figure 4.

Baroclinic mode n	**G_n - Annual cycle**	**G_n - Semiannual cycle**
1	1.39 (1.24)	0.16 (0.33)
2	0.60 (0.89)	0.21 (0.41)
3	0.13 (0.17)	0.22 (1.51)
4	0.16 (0.22)	0.07 (0.09)
5	0.14 (0.52)	0.02 (0.57)

Table 3: Dimensionless wind stress projection coefficients G_n for EF+LF simulations being forced by Fourier components of JRA55 wind stress data corresponding to annual (middle column) and semiannual (right column) oscillations as obtained from scaling model-computed amplitudes locally at 23°W-Equator. In brackets corresponding wind stress projection coefficients derived from scaling model-computed amplitudes locally at 35°W-Equator are displayed.

Baroclinic mode $\boldsymbol{n}$	Annual cycle		Semiannual cycle	
	$\boldsymbol{\Delta}$Amp. (cm s^{-1})	$\boldsymbol{\Delta}$Phase (month)	$\boldsymbol{\Delta}$Amp. (cm s^{-1})	$\boldsymbol{\Delta}$Phase (month)
1	-0.021	+5.6	+0.081	+0.11
2	+0.081	-2.3	+0.071	-0.32
3	+0.043	-0.3	+0.227	-1.0
4	-0.016	-0.4	+0.108	+0.4
5	-0.072	-1.0	+0.027	-0.2

Table 4: Amplitude and phase differences between EF-only and EF+LF simulations for individual baroclinic modes at 11°S-Angola. Positive/negative differences correspond to a stronger/weaker response to EF-only forcing compared to the EF+LF forcing, with the former inducing a southward maximum of surface alongshore velocity later/earlier, respectively. To obtain depth-dependent differences, the amplitude difference needs to be multiplied with the corresponding vertical structure function (Figure 3a).

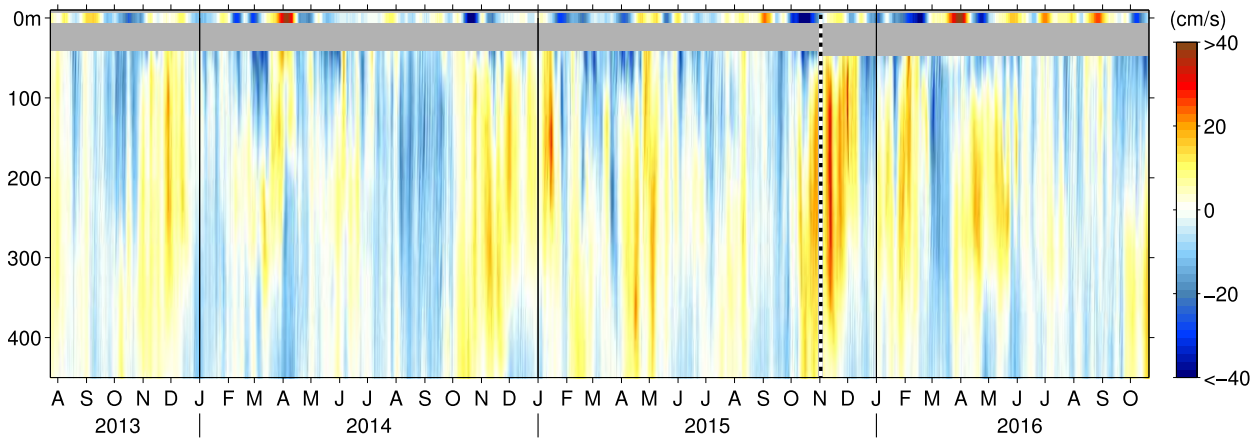

Figure 1: Time series of alongshore velocity (rotated by -34° with respect to true north) as recorded by the moored ADCP located on the 1200 m isobath off Angola (13°11.0'E, 10°50.0'S). Positive and negative values indicate equatorward and poleward flow, respectively. The vertical dashed line marks the date of the mooring redeployment. Surface values correspond to geostrophic alongshore velocities at the mooring location from altimetry.

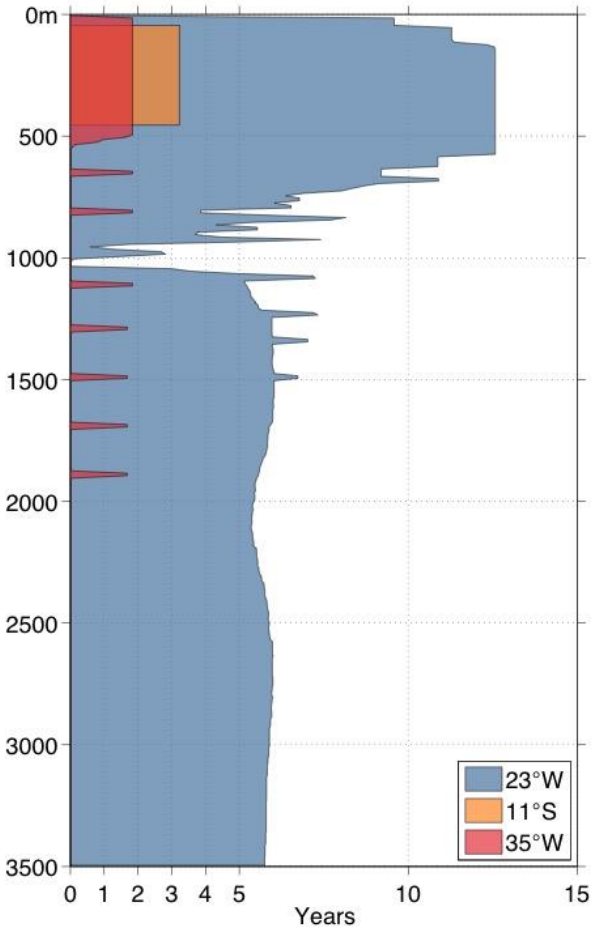

Figure 2: Length of the time series of available velocity data as function of depth for 23°W-Equator (blue), 11°S-Angola (orange), and 35°W-Equator (red).

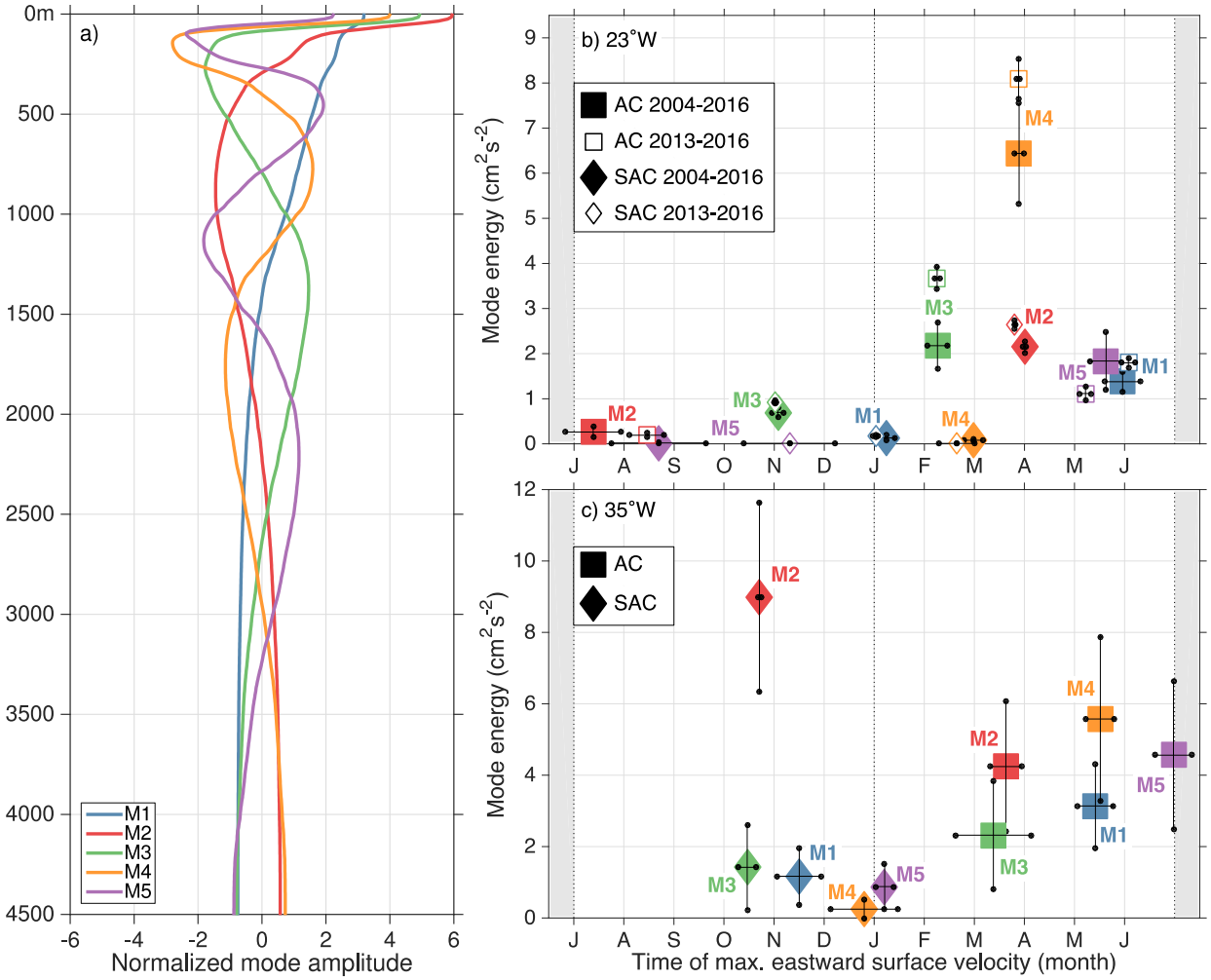

Figure 3: (a) Vertical structure functions of the first five baroclinic modes derived from a mean buoyancy frequency profile calculated from CTD profiles near 23°W-Equator. Normalization is carried out with respect to the standard deviations of the structure functions. Modal amplitudes of the energy of annual (squares, "AC") and semiannual (diamonds, "SAC") cycles of the observed zonal velocity at 23°W-Equator (b) and 35°W-Equator (c) are plotted at the mode's time of maximum eastward surface velocity. Note that, for the sake of clarity, only one of the two maxima of the semiannual cycle is shown in (b) and (c). Errorbars correspond to standard deviations of energy and phase accounting for uncertainties due to incomplete data sets (for details on the mode projection see text). In (b) mode projection is carried out considering the full

1039 length of the time series (filled symbols) as well as a subset of the time series (open symbols)
1040 that corresponds to the period of moored observations at 11°S-Angola (2013-2016).
1041

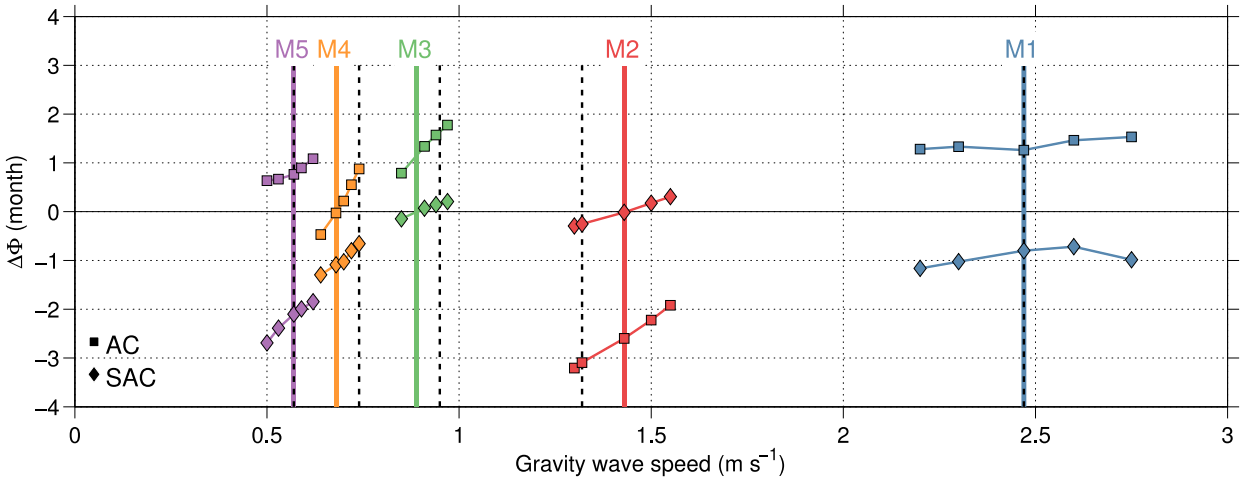

Figure 4: Local phase differences between observed and model-computed annual (squares, "AC") and semiannual (diamonds, "SAC") cycles at 23°W-Equator as function of the prescribed gravity wave speed for the first five baroclinic modes of EF+LF runs forced with JRA-55 oscillating wind stress. Vertical solid colored lines correspond to gravity wave speeds used for the remainder of the study, vertical dashed black lines are associated with theoretical gravity wave speeds used in *Brandt et al.* [2016]. See also Table 2.

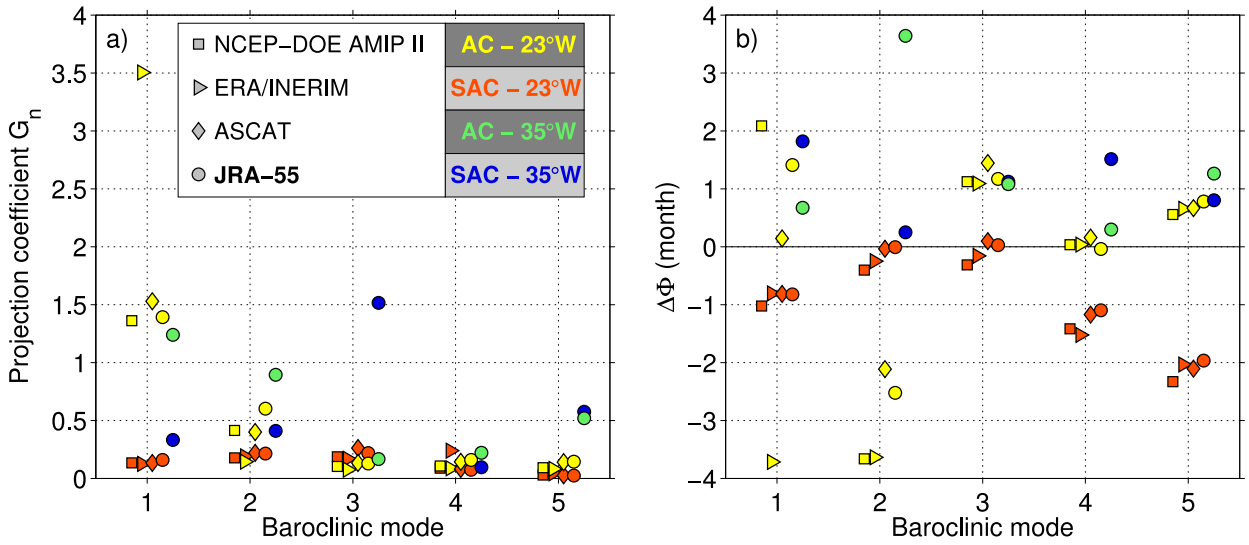

Figure 5: (a) Dimensionless projection coefficients G_n for EF+LF simulations being forced by different wind products. Projection coefficients are computed by fitting model-computed amplitudes to amplitudes derived from projecting the corresponding baroclinic mode on annual ("AC") and semiannual ("SAC") cycles of observed zonal velocity at 23°W-Equator (yellow and red, respectively), and 35°W-Equator (only shown for JRA55 forcing, green and blue, respectively). Model-computed phases are not fitted but remain solely determined by the applied wind forcing and model characteristics. In (b) local phase differences between EF+LF shallow-water model simulations and observed modal semiannual and annual cycles are shown; colors and symbols as given in (a).

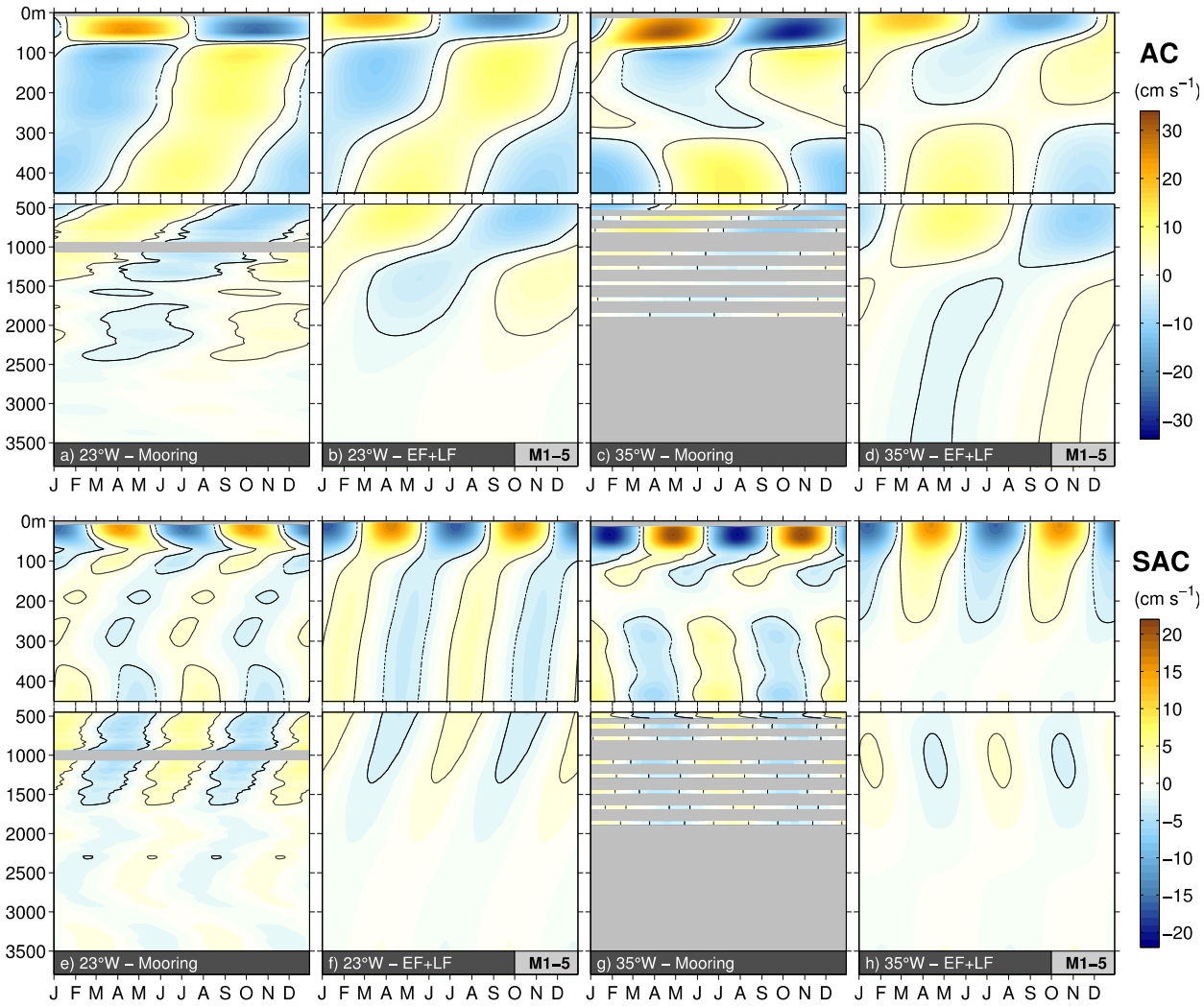

Figure 6: Annual ("AC") and semiannual ("SAC") cycles of zonal velocity (cm s^{-1}) at 23°W-Equator and 35°W-Equator as reconstructed by fitting annual (a and c) and semiannual (e and g) harmonics to the observed velocity field, and by summing up the first 5 baroclinic modes from the EF+LF shallow-water model simulations forced with annually (b and d) and semiannually (f and h) oscillating wind stress. Solid and dotted contours represent the +2 cm s^{-1} and -2 cm s^{-1} isolines, respectively. Model-computed modal amplitudes are scaled with respect to observations obtained at 23°W-Equator.

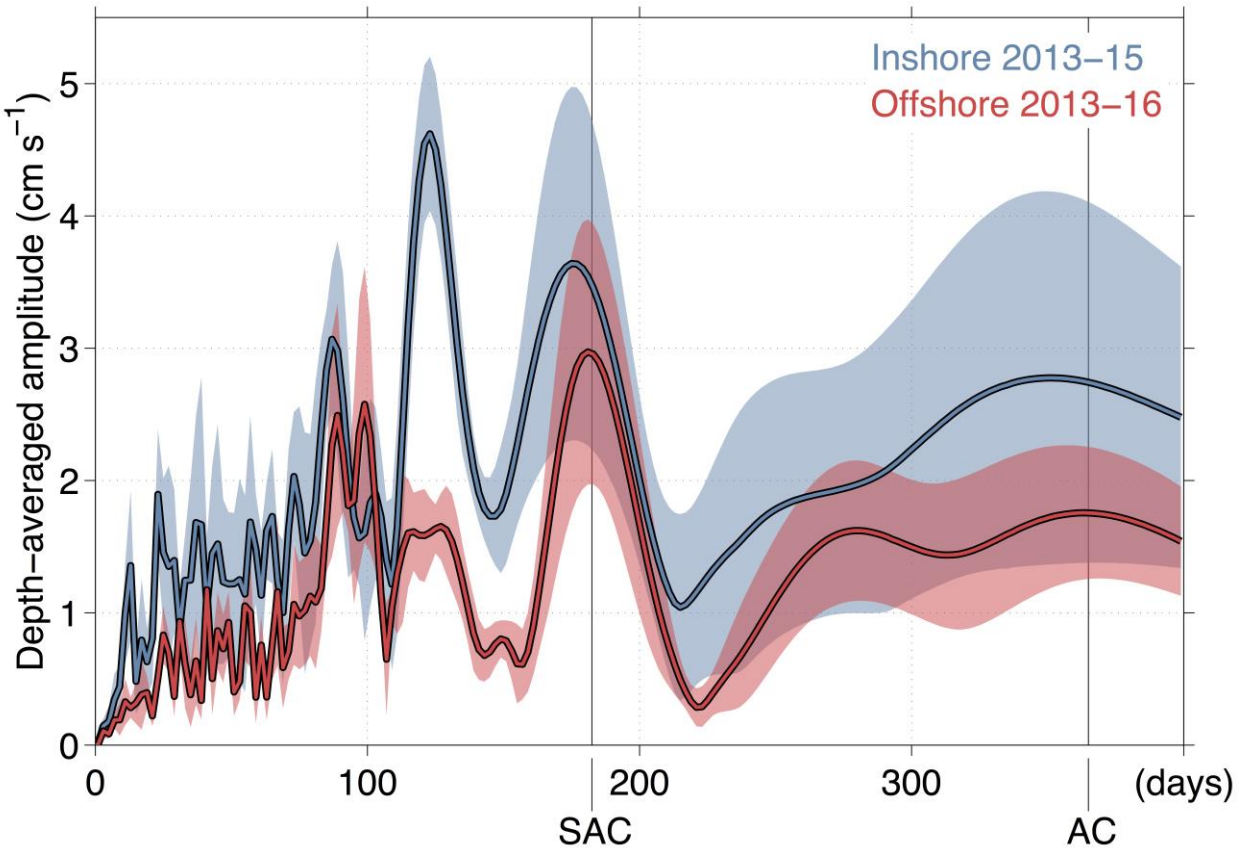

Figure 7: Mean periodograms of observed alongshore velocity at 11°S-Angola for the offshore (red, 2013-2016) and inshore (blue, 2013-2015) ADCP. Periodograms are calculated by fitting harmonic functions to the time series at each depth level between 45 and 450 m followed by vertical averaging. Shaded areas indicate standard deviations of individual periodograms with respect to depth.

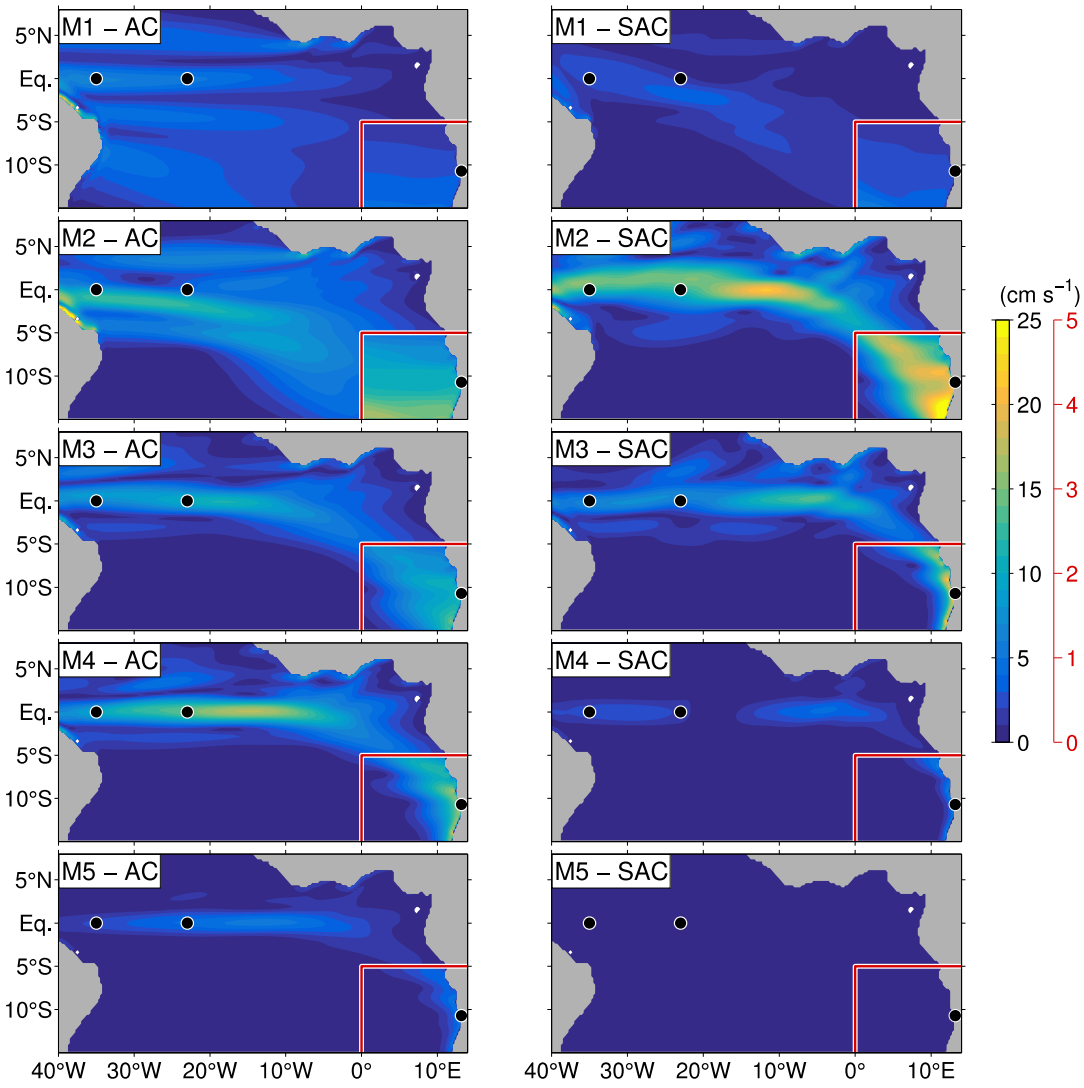

Figure 8: Amplitudes of annual (left column, "AC") and semiannual (right column, "SAC") cycles of surface zonal velocities for baroclinic modes 1-5 from the EF-only runs. Within the rectangle in the southeastern corner of the domain corresponding amplitudes of meridional velocity are shown (associated with the red color scale). Black dots denote mooring locations at 35°W-Equator, 23°W-Equator, and 11°S-Angola.

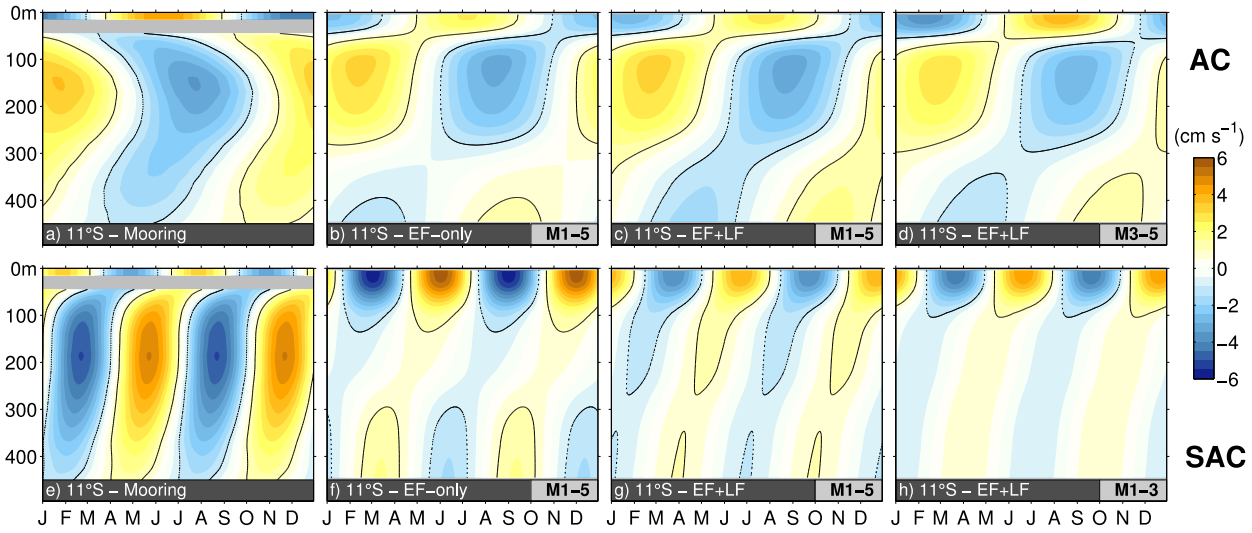

Figure 9: Baroclinic structures of observed annual (a, "AC") and semiannual (e, "SAC") oscillations of alongshore velocity at 11°S-Angola derived by fitting harmonic functions at each depth level. At the surface corresponding oscillations derived from AVISO geostrophic velocities are shown. Shown to the right are corresponding baroclinic structures obtained from the sum of the first five baroclinic modes from the EF-only simulations driven (b, f) and the EF+LF simulations (c, g). In (d) and (h) only EF+LF simulations for baroclinic modes with their resonance periods closest to either the annual or semiannual cycle are considered for the summation. Solid and dotted contours in all subplots represent the +1 cm s^{-1} and -1 cm s^{-1} isolines, respectively.

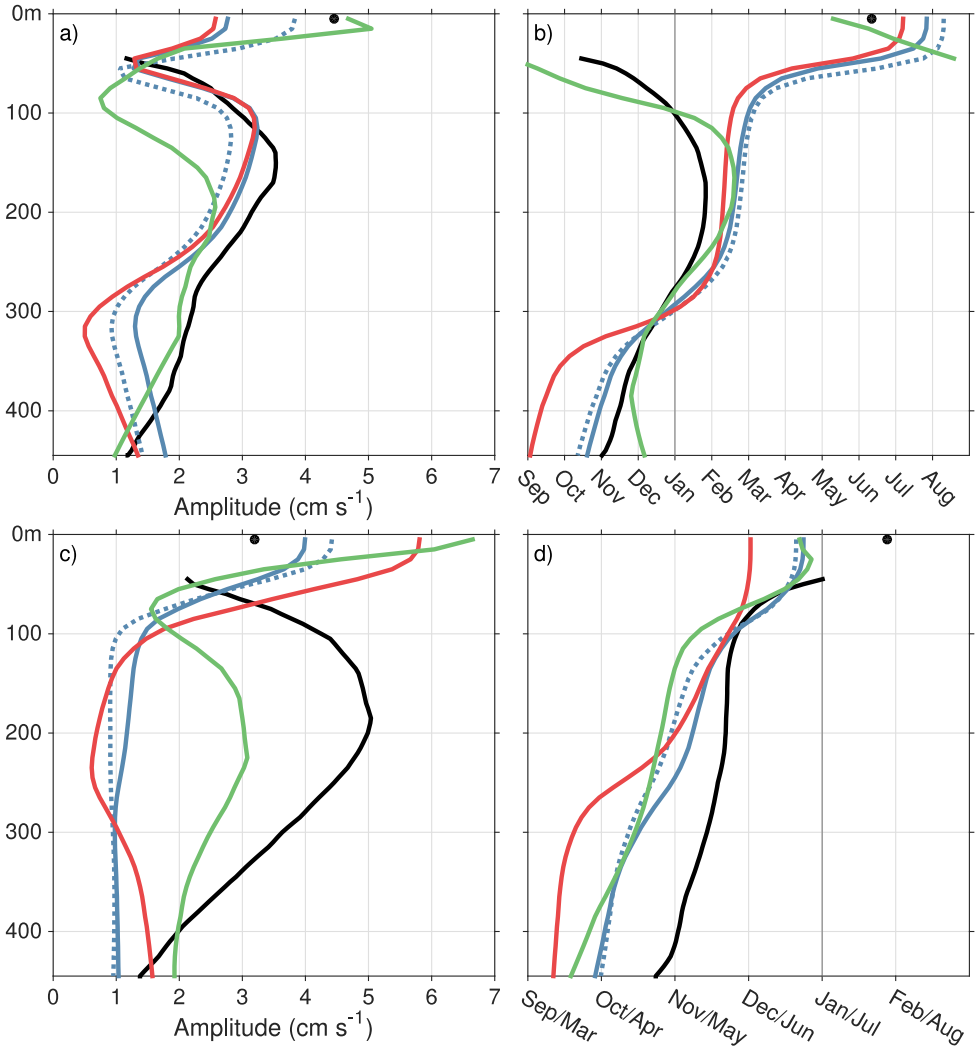

Figure 10: (left) Amplitude and (right) month of maximum northward flow, as function of depth for (a and b) annual and (c and d) semiannual cycles of alongshore velocity at 11°S-Angola corresponding to patterns in Figure 9: Observations (black), EF-only (red), and EF+LF simulations (solid blue: Modes 1-5; dotted blue: Modes 3-5 for AC, modes 1-3 for SAC). Additionally, corresponding profiles derived from TRATL01 output are shown in green.

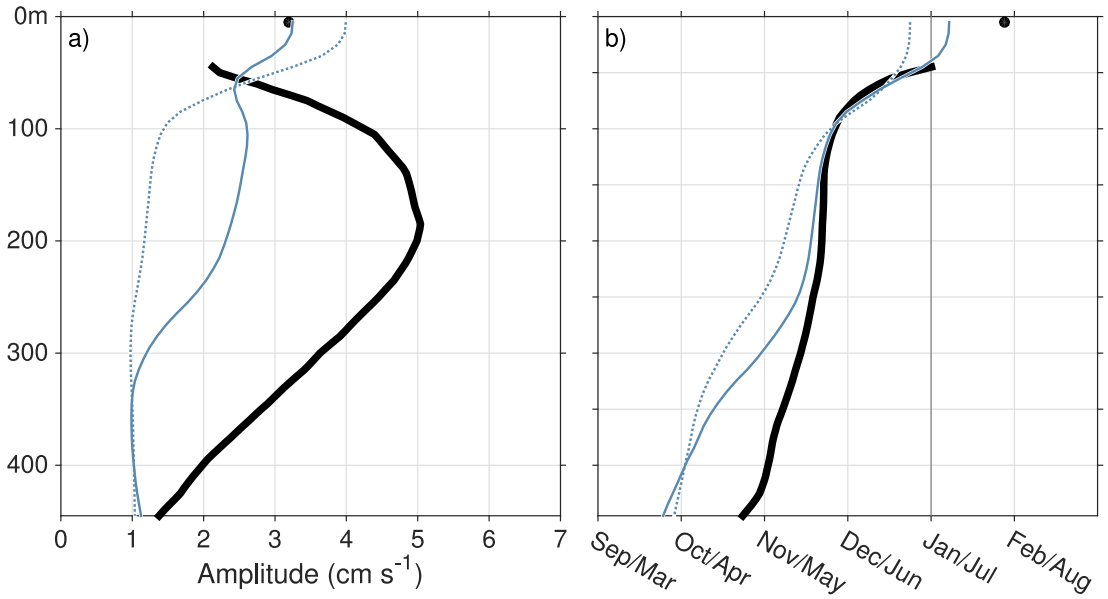

Figure 11: (a) Amplitude and (b) phase as function of depth for semiannual cycle of alongshore velocity at 11°S-Angola for observations (thick black), EF+LF simulations (dotted blue), and EF+LF simulations, where the amplitude of the fourth baroclinic mode was enhance by a factor 4.5 (solid blue)

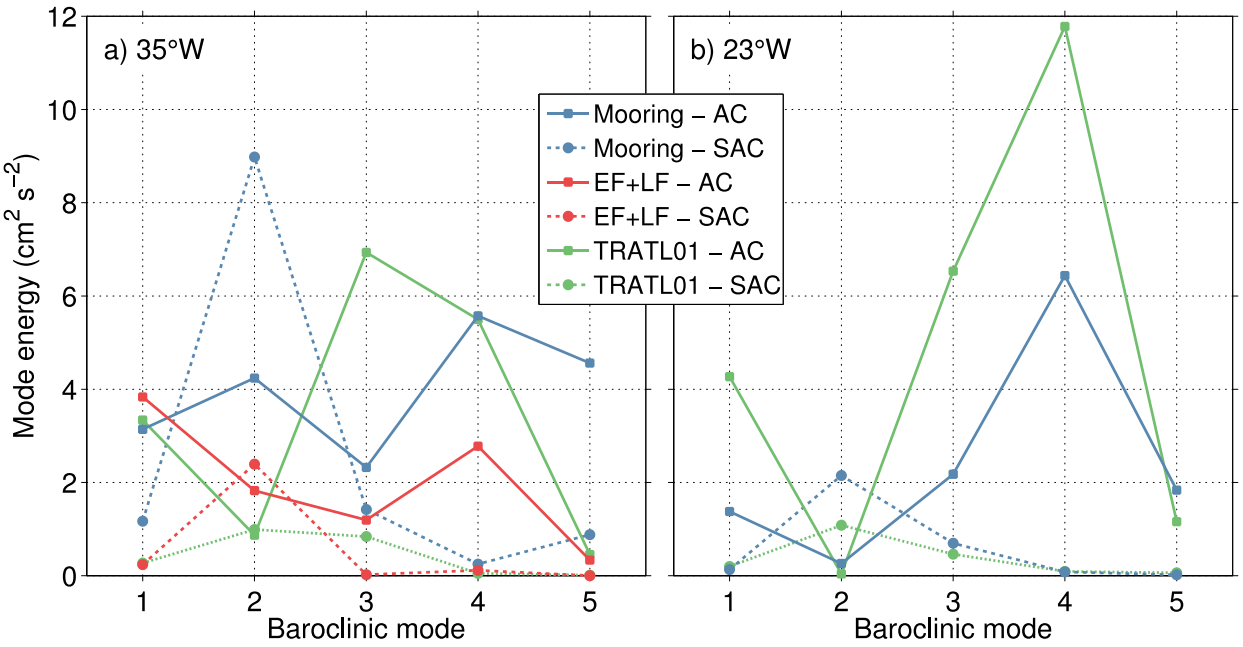

Figure 12: Baroclinic mode energy spectra of the annual (solid, "AC") and semiannual (dashed, "SAC") cycles for 35°W-Equator (a) and 23°W-Equator (b) derived from moored velocity observations (blue), EF+LF shallow-water model simulations (red), and the TRATL01 model (green). In b) mode spectra of the shallow-water model are identical to the one derived from observations as model-computed modal amplitudes are scaled locally at 23°W-Equator.

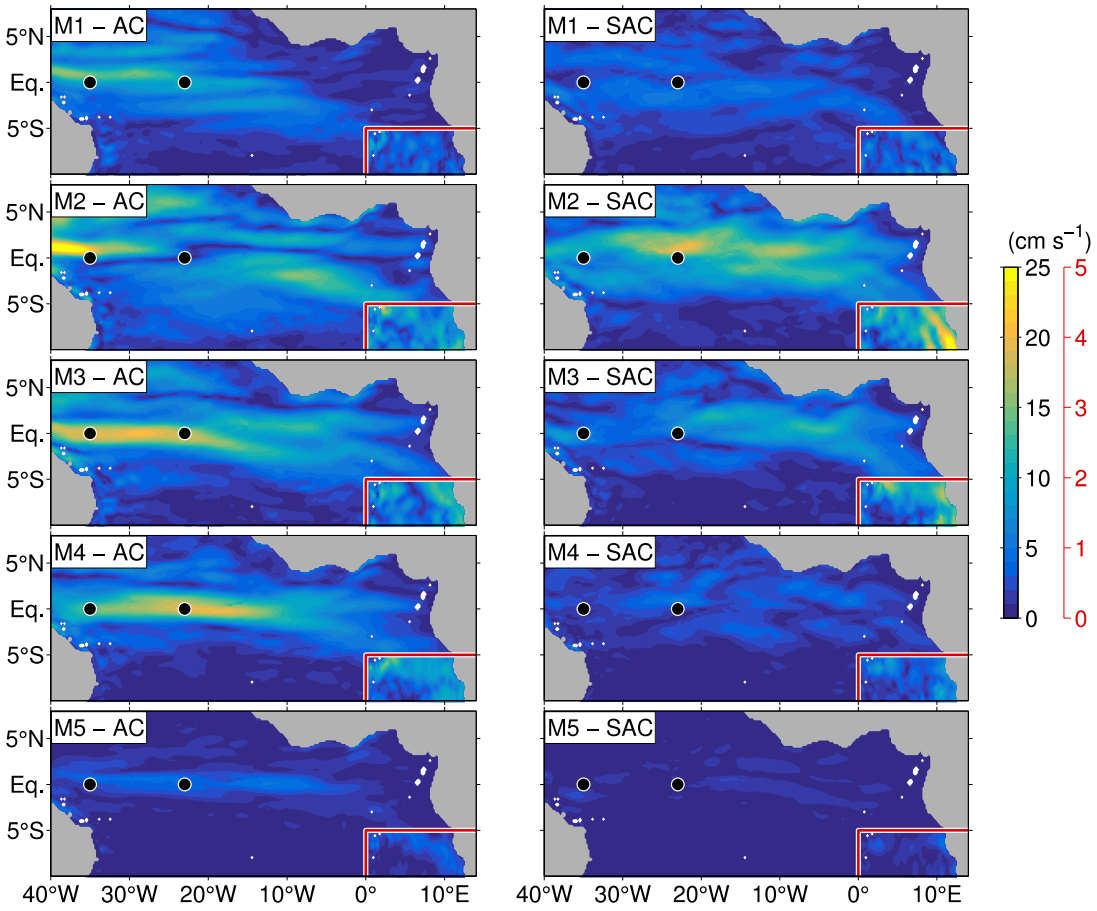

Figure 13: As Figure 8, but from the TRATL01 model. Mode projection is carried out at model grid points with water depth larger than 1000 m.